AD________________

Award Number: W81XWH-10-1-0506

TITLE: Imaging Molecular Signatures of Breast Cancer with X-ray Activated Nano-Phosphors

PRINCIPAL INVESTIGATOR: Colin M. Carpenter

CONTRACTING ORGANIZATION: The Leland Stanford Junior University
Stanford, CA 94305

REPORT DATE: September 2011

TYPE OF REPORT: Annual Summary

PREPARED FOR: U.S. Army Medical Research and Materiel Command
Fort Detrick, Maryland 21702-5012

DISTRIBUTION STATEMENT: Approved for Public Release;
Distribution Unlimited

REPORT DOCUMENTATION PAGE

Form Approved
OMB No. 0704-0188

1. REPORT DATE September 2011	**2. REPORT TYPE** Annual Summary	**3. DATES COVERED** 1 September 2010 – 31 August 2011

4. TITLE AND SUBTITLE

Imaging Molecular Signatures of Breast Cancer with X-ray Activated Nano-Phosphors

5a. CONTRACT NUMBER

5b. GRANT NUMBER
W81XWH-10-1-0506

5c. PROGRAM ELEMENT NUMBER

6. AUTHOR(S)

E-Mail: colincarpenter@stanford.edu

5d. PROJECT NUMBER

5e. TASK NUMBER

5f. WORK UNIT NUMBER

7. PERFORMING ORGANIZATION NAME(S) AND ADDRESS(ES)

The Leland Stanford Junior University
Stanford, CA 94305

8. PERFORMING ORGANIZATION REPORT NUMBER

9. SPONSORING / MONITORING AGENCY NAME(S) AND ADDRESS(ES)
U.S. Army Medical Research and Materiel Command
Fort Detrick, Maryland 21702-5012

10. SPONSOR/MONITOR'S ACRONYM(S)

11. SPONSOR/MONITOR'S REPORT NUMBER(S)

12. DISTRIBUTION / AVAILABILITY STATEMENT
Approved for Public Release; Distribution Unlimited

13. SUPPLEMENTARY NOTES

14. ABSTRACT

The first year of this research program developed the foundation for a new medical imaging modality, now called Radioluminescence Tomography (RLT), which utilizes biologically compatible phosphor nanoparticles to produce images of molecular breast cancer contrasts. The development of this modality is significant to the early detection of breast cancer, and to provide feedback to guide Radiation Therapy, for such breast cancer treatments as Intraoperative Radiation Therapy. The work in Year 1 developed sophisticated modeling imaging techniques to enable this modality; this algorithm enables higher resolution with lower dose to the internal organs. This grant resulted in the full characterization of phosphor nanoparticles (Gd_2O_2S:Eu, Tb, Pr) for RLT. This research has also successfully aided in the development of a new radioluminescent phosphor, Barium Yttrium Fluoride. This modality was demonstrated in phantoms and a mouse model. As part of the first-year training goals, this grant has provided the opportunity for extensive training in molecular targeting of cancer, molecular imaging modalities, and opportunities to engage physicians to design appropriate tools. As of today, the results of this grant are: 5 journal publications, including 2 first author, with 2 more in preparation; 8 conference abstracts, including 3 first author, and 2 conference presentations; 4 courses taken, including BioE222: Molecular Imaging, Med374: Medical Device Design (taken after the grant was accepted, but before it was funded), the Comprehensive Cancer Research Training Program, and SIE: The Stanford Institute for Entrepreneurs, and mentoring of 1 undergraduate and 1 high school student.

15. SUBJECT TERMS
BREAST CANCER, IMAGING, MOLECULAR IMAGING, X-RAY, NANOPARTICLES

16. SECURITY CLASSIFICATION OF:			**17. LIMITATION OF ABSTRACT**	**18. NUMBER OF PAGES**	**19a. NAME OF RESPONSIBLE PERSON** USAMRMC
a. REPORT U	**b. ABSTRACT** U	**c. THIS PAGE** U	UU		**19b. TELEPHONE NUMBER** *(include area code)*

Table of Contents

Page

INTRODUCTION

The goals of the first year of this training grant were to develop the foundations for a new medical imaging modality, now called Radioluminescence Tomography (RLT), which utilizes biologically compatible phosphor nanoparticles to produce images of molecular breast cancer contrasts. The development of this modality is significant to the early detection of breast cancer, because it provides additional disease-specific molecular information to X-ray mammography, which is the most widespread medical imaging modality for breast cancer screening. In addition, this modality has the potential to provide feedback to guide Radiation Therapy, for such breast cancer applications as Intraoperative Radiation Therapy. The first-year research goals were to develop a mathematical framework and the instrumentation to enable this modality, and to fabricate and fully characterize phosphor nanoparticles for RLT. In addition, this research grant has aided in the development of a new more biologically compatible radioluminescent phosphor, Barium Yttrium Fluoride, which has been thoroughly characterized, and successfully imaged in phantoms and a mouse. In addition, this grant has provided the funding to devise a more sophisticated version of RLT, Limited-Angle X-ray Luminescence Tomography, which has the potential to achieve high resolution with a decrease in X-ray dose to healthy tissue. For the first-year training goals, this grant has provided for extensive study in molecular targeting of cancer, molecular imaging modalities, and opportunities to engage physicians. As of today, the results of this grant are: 5 journal publications, including 2 first author, with 2 more in preparation; 8 conference abstracts, including 3 first author, and 2 conference presentations; 4 courses taken, including BioE222: Molecular Imaging, Med374: Medical Device Design (taken after the grant was accepted, but before it was funded), the Comprehensive Cancer Research Training Program at Stanford, and SIE: The Stanford Institute for Entrepreneurs, and mentoring of 1 undergraduate and 1 high school student. The future for this grant looks bright, as this technique will soon be tested in small-animal models *in vivo*; the next, more clinically feasible interventional version is under development.

BODY

Research Accomplishments: SOW Aim 1: Nanophosphor characterization

The feasibility of X-ray luminescence with Gadolinium oxysulfide particles was investigated. We examined the practical aspects of this new modality, including phosphor concentration, light emission linearity, detector damage, and spectral emission characteristics. Finally, the contrast produced by these phosphors was compared to that of X-ray fluoroscopy.

Gadolinium and lanthanum oxysulfide phosphors doped with terbium (green) or europium (red) were studied. The light emission was imaged in a clinical X-ray scanner with a cooled CCD camera and a spectrophotometer; dose measurements were determined with a calibrated dosimeter. Using these properties in addition to luminescence efficiency values found in the literature for a similar phosphor, minimum concentration calculations were performed. Finally, a 2.5cm agar phantom with a 1cm-diameter cylindrical phosphor-filled inclusion (diluted at 10mg/ml) was imaged to compare X-ray luminescence contrast with X-ray fluoroscopic contrast at a superficial location.

Dose to the CCD camera in the chosen imaging geometry was measured at less than 0.02cGy/sec. Emitted light was found to be linear with dose ($R^2 = 1$) and concentration ($R^2=1$). Phosphor emission peaks were less than 3nm full-width at half-maximum, as was expected from lanthanide dopants. The minimum practical concentration necessary to detect luminescent phosphors was dependent on dose; it was estimated that sub-picomolar concentrations are detectable at the surface of the tissue with typical mammographic doses, with the minimum detectable concentration increasing with depth and decreasing with dose. In a reflection geometry, X-ray luminescence had nearly a 430-fold greater contrast to background than X-ray fluoroscopy.

The outcome of this aim was a successful demonstration and feasibility assessment of this modality using Gadolinium Oxysulfide. However, due to difficulties in making these phosphors biocompatible, the phosphors were switched to $BaYF_4$, which may be more easily bioconjugated and tagged to molecular markers. Indeed, in a preliminary study, these phosphor were targeted to the Folate receptor (commonly expressed in breast cancer), and uptaken by live cells (data not shown).

Training Accomplishments: SOW Aim 1: Nanophosphor characterization
In performing these tasks, the investigator has been exposed to the field of molecular imaging, a new direction for this PI. This research education has been aided with participation in BioE222: Molecular Imaging, which brought together the top molecular imaging faculty at Stanford to teach aspects in the hardware, chemistry, and biology of molecular imaging. In addition, the PI was exposed to nanoparticle fabrication, including the processes in making nanoparticles stable in human serum with low toxicity. Also, the PI gained knowledge in molecular targets, and the advantages and disadvantages of targeting to peptides, hormones, antibidies, affabodies, and other targeting agents. This program has been aided by working at benchside with these materials scientists, biologists, and nuclear imaging experts.

Research Accomplishments: SOW Aim 2: Imaging Hardware Development
This aim extended the ability of Radioluminescent Imaging with the construction of a fully functioning system, shown in Figure 1, which has full spectral and imaging capabilities to image small-animals injected with nanophosphors with high resolution. In addition, this aim resulted in the development of a novel algorithm which incorporated a diffuse optical photon propagation model into the reconstruction algorithm to recover unresolved dimensions in an X-ray limited angle (LA) geometry. This sophisticated technique enables such applications as image-guided surgery, where the ability to resolve lesions at depths of several centimetres, which can be the key to successful resection. In addition, the internal organs need not be irradiated. The hybrid X-ray / diffuse optical model was formulated and demonstrated in a breast-sized phantom, simulating a breast lumpectomy geometry. Both numerical and experimental phantoms were tested, with lesion-simulating objects of various sizes and depths. Results showed localization accuracy with median error of 2.2mm, or 4% of object depth, for small 2-14mm-diameter lesions positioned from 1cm to 4.5cm in depth. This compares favorably with fluorescence optical imaging, which is not able to resolve such small objects at this depth. The recovered lesion size had lower size-bias in the X-ray excitation direction than the optical direction, which was expected due to the optical scatter. However, the technique was shown to be quite invariant in recovered size with respect to depth, as the standard deviation was less than 2.5mm. Sensitivity was a function of dose; radiological doses were found to provide sufficient recovery for μg/ml concentrations, while therapy dosages provided recovery for ng/ml

Figure 1: Small-animal imaging box fabricated to provide proof-of-concept and aid in technique and nanoparticle development.

concentrations. Experimental phantom results agreed closely with the numerical results, with positional errors recovered within 8.6% of the effective depth for a 5mm object, and within 5.2% of the depth for a 10mm object. Object size median error was within 2.3% and 2% for the 5mm and 10mm objects, respectively. For shallow-to-medium depth applications where optical and radio-emission imaging modalities are not ideal, such as in intra-operative procedures, this new technique, LAXLT, may be a useful tool to detect molecular signatures of disease. For this aim, the software and hardware proof-of-principle experiments were performed.

Training Accomplishments: SOW Aim 2: Imaging Hardware Development

In performing these tasks, the investigator explored various methods of multimodality imaging, by fusing X-ray and optical photon propagation models. This work was carried out under guidance from Dr. Lei Xing, as proposed, who is an expert in X-ray modeling in tissue. A numerical photon propagation model was built, and integrated into the PI's existing code for optical photon modeling. The system development for pre-clinical imaging was a first for this PI: a small-animal system devoted to testing modality feasibility, and one that may have potential for high-resolution small-animal imaging.

KEY RESEARCH ACCOMPLISHMENTS

- Established the feasibility of Radioluminescent Tomography in reflection mode.
- Developed a hybrid X-ray/Optical photon propagation model to perform high resolution Radioluminescent Tomography, in an appropriate geometry for Intraoperative Radiation Therapy.
- Characterized nanophosphors suitable for RLT, including Gadolinium oxysulfide and Barium Yttrium Fluoride.
- Fabricated a small-animal pre-clinical RLT imaging box to enable automated, controlled, RLT experiments.

REPORTABLE OUTCOMES

5 journal publications, including 2 first author, with 2 more in preparation; 8 conference abstracts, including 3 first author, and 2 conference presentations; 4 courses taken, including BioE222: Molecular Imaging, Med374: Medical Device Design (taken after the grant was accepted, before it was funded), the Comprehensive Cancer Training Program, and SIE: The Stanford Institute for Entrepreneurs, and 1 undergraduate and 1 high school student mentored (again after the grant was accepted, but before it was funded). 1 patent application.

Oral Presentations:

- **Carpenter, CM**., et al.. "Intraoperative Breast Radiotherapy guided by X-ray Luminescent Nanoparticles," Presented at Novel Treatment Delivery Techniques, American Society for Therapeutic Radiology and Oncology, San Diego, CA, Nov. 2010.
- **Carpenter, CM**. "Development of An X-Ray/Optical Luminescence Imager for Improved X-Ray Contrast Sensitivity", Presented at the 52nd Annual Meeting of the AAPM, Philadelphia, PA, July, 2010.

Journal Publications:

- **Carpenter CM**., et al. “Limited-Angle X-ray Luminescence Tomography: Methodology and Feasibility Study” Phys Med Biol, 2011.
- **Carpenter CM**., et al. “X-ray/Optical Luminescence Imaging; Characterization of Experimental Conditions,” Med Phys, 37(8) 2010.
- Sun C, Pratx G, **Carpenter CM**, Liu H, Cheng Z, Gambhir SS, Xing L. Synthesis and Radioluminescence of PEGylated Eu3+-doped Nanophosphors as Bioimaging Probes Advanced Materials, in press.
- Sun C**, Carpenter CM**, Pratx G, Xing L. Facile synthesis of amine functionalized Eu3+-doped La(OH)3 nanophosphors for bioimaging Nanoscale Research Letters, 6(24) 2011.
- Pratx, G., Carpenter, CM., et al., “Tomographic Molecular Imaging using X-ray Excitable Nanoparticles., Opt. Lett., 35(20) 3345-7, 2010.

CONCLUSION

The first funding period in this grant has developed the research infrastructure for Radioluminescence Tomography. This has resulted in a fully functioning system that may perform the systematic studies in phantoms and pre-clinical animals that is the crux of Aims 3 & 4 from the SOW. Towards the goal of determining the feasibility for patient imaging, imaging fiber optic bundles have been purchased which are compatible with the current system, and will provide proof-of-concept for the mammographic and needle-biopsy realizations of this modality. Future work for Aims 3&4 will involve a more sophisticated phantom study to evaluate system temporal and sensitivity performance with regards to imperfect background contrast uptake, and a systematic study to determine the feasibility in pre-clinical and clinical research. In addition, the first funding period for this grant resulted in much training for the PI, for molecular imaging, small-animal imaging, cancer biology, and device commercialization.

The research and training in the grant are significant for the eradication of breast cancer for the new developments in the potential for early detection of breast cancer, for the treatment of breast cancer by providing feedback to guide Radiation Therapy, for such breast cancer applications as Intraoperative Radiation Therapy, and for the coursework which will enable this PI to apply newly learned skills to bring technologies to the clinic and marketplace. It is our hope that this pioneering work will lead to advancements in this new field that can be translated to the clinic.

REFERENCES

- **Carpenter CM**., et al. “Limited-Angle X-ray Luminescence Tomography: Methodology and Feasibility Study” Phys Med Biol, 2011.
- **Carpenter CM**., et al. “X-ray/Optical Luminescence Imaging; Characterization of Experimental Conditions,” Med Phys, 37(8) 2010.
- Sun C, Pratx G, **Carpenter CM**, Liu H, Cheng Z, Gambhir SS, Xing L. Synthesis and Radioluminescence of PEGylated Eu3+-doped Nanophosphors as Bioimaging Probes Advanced Materials, in press.
- Sun C**, Carpenter CM**, Pratx G, Xing L. Facile synthesis of amine functionalized Eu3+-doped La(OH)3 nanophosphors for bioimaging Nanoscale Research Letters, 6(24) 2011.
- Pratx, G., Carpenter, CM., et al., “Tomographic Molecular Imaging using X-ray Excitable Nanoparticles., Opt. Lett., 35(20) 3345-7, 2010.

APPENDIX

Hybrid x-ray/optical luminescence imaging: Characterization of experimental conditions

C. M. Carpenter,[a] C. Sun, and G. Pratx
Department of Radiation Oncology, School of Medicine, Stanford University, Stanford, California 94305

R. Rao
SRI International, Menlo Park, California 94025

L. Xing
Department of Radiation Oncology, School of Medicine, Stanford University, Stanford, California 94305

(Received 21 April 2010; revised 28 May 2010; accepted for publication 6 June 2010; published xx xx xxxx)

Purpose: The feasibility of x-ray luminescence imaging is investigated using a dual-modality imaging system that merges x-ray and optical imaging. This modality utilizes x-ray activated nanophosphors that luminesce when excited by ionizing photons. By doping phosphors with lanthanides, which emit light in the visible and near infrared range, the luminescence is suitable for biological applications. This study examines practical aspects of this new modality including phosphor concentration, light emission linearity, detector damage, and spectral emission characteristics. Finally, the contrast produced by these phosphors is compared to that of x-ray fluoroscopy.
Methods: Gadolinium and lanthanum oxysulfide phosphors doped with terbium (green) or europium (red) were studied. The light emission was imaged in a clinical x-ray scanner with a cooled CCD camera and a spectrophotometer; dose measurements were determined with a calibrated dosimeter. Using these properties, in addition to luminescence efficiency values found in the literature for a similar phosphor, minimum concentration calculations are performed. Finally, a 2.5 cm agar phantom with a 1 cm diameter cylindrical phosphor-filled inclusion (diluted at 10 mg/ml) is imaged to compare x-ray luminescence contrast with x-ray fluoroscopic contrast at a superficial location.
Results: Dose to the CCD camera in the chosen imaging geometry was measured at less than 0.02 cGy/s. Emitted light was found to be linear with dose ($R^2=1$) and concentration ($R^2=1$). Emission peaks for clinical x-ray energies are less than 3 nm full width at half maximum, as expected from lanthanide dopants. The minimum practical concentration necessary to detect luminescent phosphors is dependent on dose; it is estimated that subpicomolar concentrations are detectable at the surface of the tissue with typical mammographic doses, with the minimum detectable concentration increasing with depth and decreasing with dose. In a reflection geometry, x-ray luminescence had nearly a 430-fold greater contrast to background than x-ray fluoroscopy.
Conclusions: X-ray luminescence has the potential to be a promising new modality for enabling molecular imaging within x-ray scanners. Although much work needs to be done to ensure biocompatibility of x-ray exciting phosphors, the benefits of this modality, highlighted in this work, encourage further study.
[DOI: 10.1118/1.3457332]

I. INTRODUCTION

Molecular imaging promises increased sensitivity and specificity to disease compared to traditional anatomical imaging modalities. The information gained from molecular imaging has the potential to provide patient-specific selection of therapy, improved prediction of outcomes, and increased treatment efficacy.[1] X-ray radiography and computed tomography (CT) are commonly used anatomical imaging modalities; however, although they provide invaluable information in the clinic, they have been largely unsuccessful for molecular imaging.[2] This deficiency is due to their lack of sensitivity to low concentrations of contrast agents; x-ray imaging is commonly believed to be many orders of magnitude less sensitive than optical[3] or radionuclide[4] imaging. This poor sensitivity arises from the low x-ray stopping power of diluted contrast agents, which necessitates high concentrations compared to other imaging modalities.[2]

Phosphors are well-established materials used universally in cathode ray tubes and light-emitting diodes for their ability to emit light upon excitation by electrons or photons. Phosphors consist of solid-state crystals, which are typically doped with transition metals or lanthanide ions. These materials form a system optimized to capture higher-energy radiation and emit downconverted energy as optical photons. In the context of an x-ray scanner, x-ray photons transfer some or all of their energy to electrons in the solid-state crystal through Compton and photoelectric interactions.[5] These high-energy electrons progressively lose energy through interactions with the atoms, leaving a track of excited electrons

behind. When the energy of the excited electrons in the conduction band is reduced to approximately two to three times the band gap, they may migrate into the luminescence center of the phosphor, the dopant, and recombine with holes to emit light.[6] Thus, this amplification process results in effective quantum efficiencies (photons emitted divided by the photons absorbed), which can be much greater than 1. For example, on the average, 6000 photons are produced for each 100 keV x-ray photon absorbed in one particular gadolinium oxysulfide:terbium phosphor.[7] The emitted light may then be imaged by sensitive optical detectors.

This paper investigates the use of nanosized inorganic phosphors[7] as potential biological contrast agents for medical imaging in a combined x-ray/optical instrument. The emission from this contrast agent is evaluated to determine the practicality of this new modality. The implications for this x-ray activated contrast agent are discussed with regard to its potential to enable molecular imaging during fluoroscopy, x-ray CT, or projection x-ray imaging.

II. METHODS

II.A. Phosphor fabrication

Trivalent europium (Eu) or terbium (Tb) activated gadolinium oxysulfides (GOSs) or lanthanum oxysulfides (LOSs) were synthesized using appropriate rare earth nitrates (99.99% pure) with two standard methods: The gel-polymer combustion process and the combination capping process,[6] respectively. After preparation, samples were heat treated at 500–600 °C for 1–3 h to aid the migration of the dopant into the crystal lattice structures. Next, the powders were ball milled with glass beads (10 μm) in the presence of the appropriate surfactant for 2–3 h.

II.B. Spectroscopy and imaging of phosphor characteristics

To facilitate spectroscopy and imaging for the analysis of the properties of the phosphors, dry phosphor was placed in plastic test tubes. For spectroscopy, the distal end of a 10 m–400 μm optical fiber was placed in contact with the side of the test tube, while the proximal end was attached to a spectrophotometer (Jaz, Ocean Optics, Dunedin, FL), which was operated from the x-ray control room. Optical emission spectra across the visible and near infrared (NIR) range were acquired with the SPECTRASUITE (Ocean Optics) software package. Imaging was performed with a 512×512 pixel backilluminated CCD camera (CCD temperature maintained at −70 °C) with a F1.4 imaging lens, exposure times varying from <1 to 60 s, and the lens aperture fully open. During data acquisition, the imaging camera was shielded with lead bricks and placed 15–20 cm outside the direct field of radiation to protect from ionizing radiation. The optics setup was placed inside a light-tight box to eliminate ambient room light. A schematic of this imaging setup is shown in Fig. 1(a), and a photograph of the setup during experimental imaging is shown in Fig. 1(b).

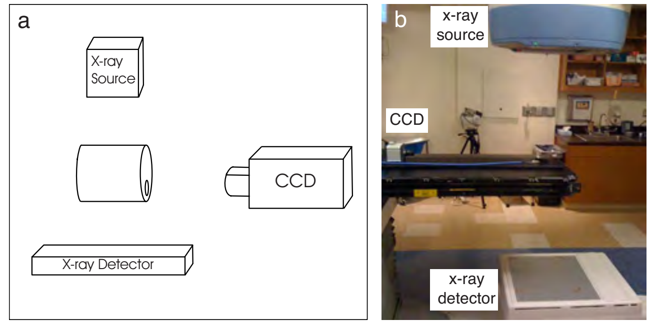

FIG. 1. (a) Schematic of the experimental setup including the CCD camera, the x-ray source and detector, and the sample. (b) Photograph of the imaging setup.

A cone beam computed tomography (CBCT) system (Acuity, Varian Medical Systems, Palo Alto, CA) was used to irradiate the sample. This system allows both CBCT and fluoroscopy at various tube voltages between 70 and 125 kV. This system was operated in fluoroscopy mode to enable continuous irradiation from a constant geometry.

II.C. Concentration evaluation

Minimum detectable concentrations were calculated, assuming a superficial location of the phosphor contrast agent (i.e., no signal loss due to tissue absorption). Including light detection losses L, the light detected Φ is

$$\Phi = \Gamma \cdot D \cdot c \cdot L, \quad (1)$$

where Γ is the emitted light efficiency, D is the dose, and c is the concentration of the phosphor. From Ref. 8, the emitted light efficiency (in a lanthanum oxysulfide:terbium phosphor) is 1.39×10^{15} optical photons/(Gy mg). We assumed 99% detection loss due to suboptimal optical collection geometry. Signal below a signal-to-noise ratio (SNR) of 10 (assuming shot-noise limited detection) was assumed to be too low to detect. To calculate the molar concentration, we assumed a spherical 10 nm diameter nanoparticle consisting of hexagonal-structured phosphors with lattice constants of $a = 4.046$ Å and $c = 6.951$ Å (Ref. 9) and density of 5.5 g/cm^3.[10]

II.D. Optical phantom fabrication and imaging

A small-animal sized tissue-simulating phantom was fabricated for this study. The cylindrical phantom measured 2.5 cm in diameter×4.5 cm in height, with a 1×2.5 cm^2 cylindrical inclusion. The phantom was made from 1% agar with homogeneous optical properties using titanium oxide for scatter and India Ink for absorption using methods common to diffuse optical phantoms.[11] The optical properties were determined by a previously established system[12] to be $\mu_a = 0.0025$ mm^{-1} and $\mu_s' = 0.77$ mm^{-1} at 630. Micrometer-sized GOS:Eu phosphor particles were added to the inclusion at a concentration of 10 mg/ml, and no phosphor was added to the background. This phantom was imaged with an electron multiplied (EM)-CCD (Hamamatsu ImageEM 9100-13, Hamamatsu, Japan) with a 512

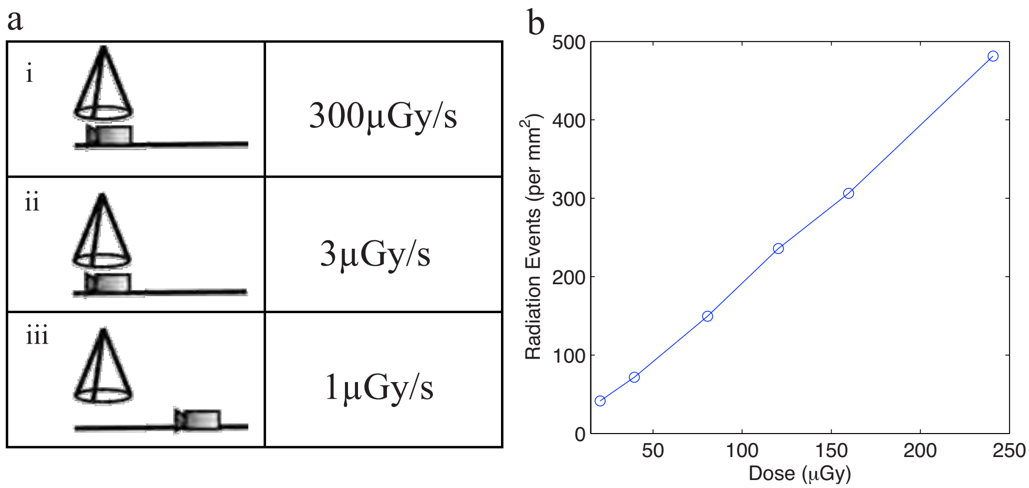

FIG. 2. (a) Radiation dose on detector for three different configurations: (i) Direct irradiation, (ii) direct irradiation with lead shielding (5 mm on top, 50 mm on each side), and (iii) indirect irradiation with lead shielding. (b) Radiation events per area per dose.

$\times 512$ pixel sensor cooled at $-70\ ^\circ C$, with a F1.4 imaging lens, with exposure of times less of 2 s, gain at half-maximum, and the lens aperture fully open.

III. RESULTS

III.A. CCD interaction with ionizing radiation

To ensure that the CCD camera would not be damaged from the ionizing radiation, an ionization chamber (PTW Farmer 30010, PTW Freiberg GMBH, Germany) was placed in the radiation field to determine the dose to air in the vicinity of the CCD. Several locations along the patient bed were measured to determine dose rate, as indicated in Fig. 2(a). Under direct radiation, the dose was nearly 300 μGy/s; this dose rate was reduced by two orders of magnitude by placing lead around the chamber, and further by twofold, to 1.5 μGy/s, by moving the chamber 15 cm out of the radiation field. This rate deposits dose well below levels that would likely damage the CCD.

To investigate camera damage further, we investigated the lingering effects of radiation on the CCD. The interaction of an x-ray photon with the CCD camera appears in the image as a bright pixel at near-maximum intensity. These hot pixels appear similar to cosmic ray interactions, which are common with CCD cameras. We investigated the incidence of these events for a typical setup using a CCD to radiation field distance of 15 cm and 6 mm of lead shielding above the camera to protect from x-ray collimator leakage. Radiation events were determined by performing an intensity threshold on an image acquired with the lens cap on. It is clear from Fig. 2(b) that the number of radiation events is linear with dose, and thus there were no lingering effects from the radiation. To improve image quality, denoising strategies may be employed utilizing this linearity, such as an automatic selection of a hot-pixel threshold, which is dependent on camera dose. Further consideration of the damage limits of CCD cameras is given in Sec. IV.

III.B. Phosphor characterization

III.B.1. Spectral emission

A large body of knowledge exists on phosphors due to over a half-century of study of optimizing phosphors for such applications as light-emitting diodes, cathode ray tubes, and scintillators for medical imaging. This work has resulted in a library of crystals and dopants from which one may select an emission wavelength that is ideal for a particular application.[6] We investigated the feasibility of GOS phosphors, which were doped with either terbium (GOS:Tb) or europium (GOS:Eu), because of their absorption K-edge in the diagnostic energy regime at approximately 50 keV.[13] Figure 3(a) shows the emission of these phosphors under 100 kV x-ray irradiation. The GOS:Tb phosphor had a maximum peak emission of 545 nm in green, whereas the GOS:Eu phosphor had several peaks of longer wavelengths in the NIR, including 596, 618, 627, and 707 nm, with an emission maximum at 627 nm. The flexibility enabled by modifying the dopant is of great value for matching the emission wavelength to a particular application, such as the absorption peak of a phototherapeutic drug,[14] or the tissue absorption minimum for optical imaging in deep tissue.[15]

III.B.2. Light output vs dose

To determine the linearity of light output from phosphor, GOS:Tb was dispersed in a cuvette containing 1% agar at a concentration of 10 mg/ml. The phosphor solution was placed at the same source-target distance as the ionization chamber. The x-ray system was operated in fluoroscopy mode and the tube voltage was set to 100kV. The dose was linearly increased by two methods. First, the tube current was increased from 5 to 20 mA with a constant tube voltage. Second, the tube voltage and current remained constant, and dose was linearly increased by adjusting the irradiation time. Images were acquired with a CCD camera, with the exposure

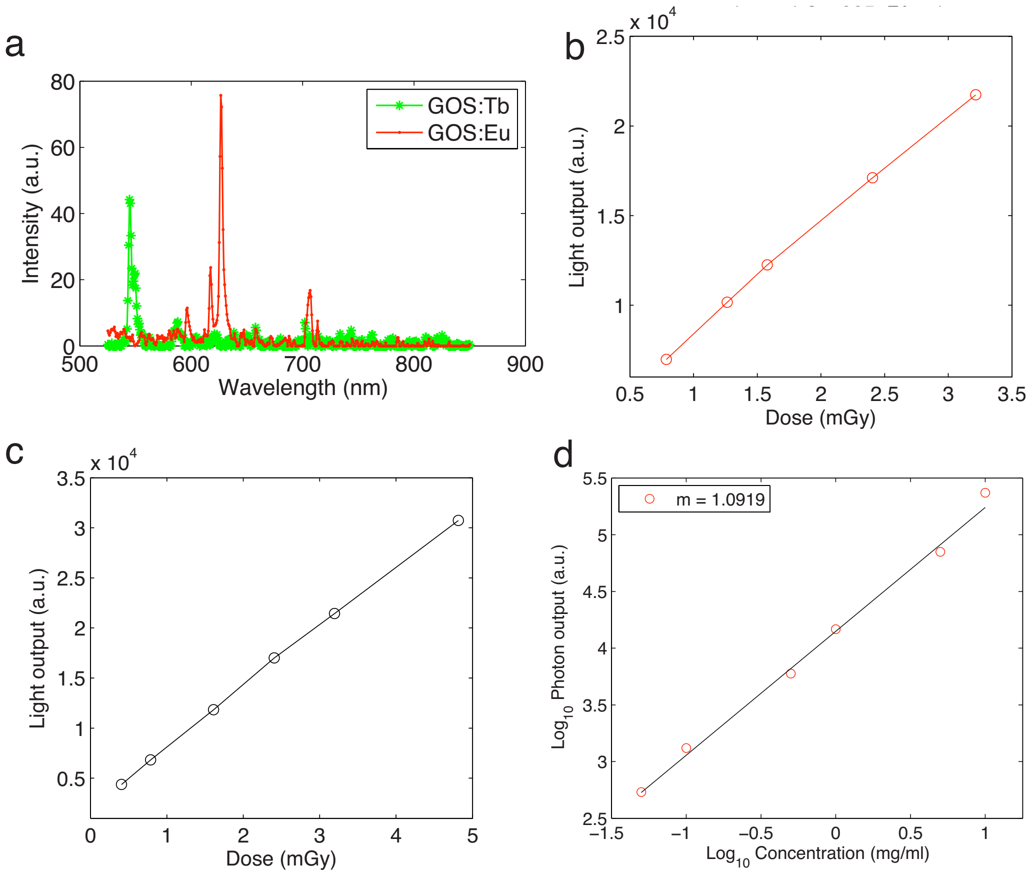

FIG. 3. (a) Emission spectra of GOS phosphors under x-ray excitation. GOS:Tb, with an emission peak at 545 nm, is labeled with asterisks (*), and GOS:Eu, with emission peaks at 596, 618, 627, and 707 nm. (b) X-ray induced GOS:Tb Photon output vs dose with dose varied by increasing tube current. (c) Photon output vs dose with dose varied by increasing irradiation time. For both methods, photon output is linear with dose shown in terms of current ($r=1$, $p<0.001$, $R^2=1$). (d) Photon output vs concentration for the GOS:Eu phosphor. Concentrations were measured via microcuvette and dispersed in 1% agar. Photon output is linear with concentration ($r=0.99$, $p=1.9\times10^{-7}$).

time optimized. All measurements were denoised for hot spots and identical regions of interest (ROIs) were selected for analysis.

AQ: #3 Both current/dose and time/dose linearity were confirmed by running a linear correlation analysis (correlation coefficient of 1.0, $p<0.001$). Figure 3(b) shows the linearity in dose using the first method, which showed significant linearity (correlation coefficient of 1.0, $p<0.001$), while Fig. 3(c) confirms linearity with the second method (correlation coefficient of 1.0, $p<0.001$).

III.B.3. *Light output vs concentration*

To assess the light output due to various phosphor concentrations, dilutions of GOS:Eu phosphors from 5 μg/ml to 10 mg/ml were dispersed in 1% agar. Cuvettes were placed in a 50 kV, 30 mA x-ray source and imaged with a CCD camera. ROIs were selected to contain similar areas of the cuvettes, and the signal was normalized according to exposure time. Hot spots were removed from the images prior to analysis.

The results shown in Fig. 3(d) demonstrate a strong linearity (linear correlation coefficient of 0.99, $p<0.001$) with a slope of 1.09. The slight departure of the slope from unity is most likely due to errors in selecting identical ROIs for the different cuvettes and may have resulted in the inclusion of the cuvette wall in the ROI, which exhibited some light piping.

III.C. Minimum detectable concentrations

We calculated the minimum detectable concentration according to the methodology outlined in Sec. II C, for doses ranging from 1 cGy (less than the typical mammographic dose) to 20 Gy (a typical dose delivered in single-dose intraoperative radiation therapy). In addition, we calculated the minimum detectable concentration for several phosphor efficiencies, scaled according to that reported by Kandarakis *et al.*[8] (i.e., 100% is equivalent to the efficiency reported). Figure 4 shows the minimum detectable concentrations for these scenarios. According to these calculations, picomolar (ng/ml) concentrations are detectable (SNR of 10) with a LOS phosphor for mammographiclike dose, while therapy doses allow femtomolar (pg/ml) concentrations to be detected.

III.D. Contrast comparison between x-ray/optical and fluoroscopy

The recovered contrast between an inclusion with phosphor and a background without phosphor was investigated to

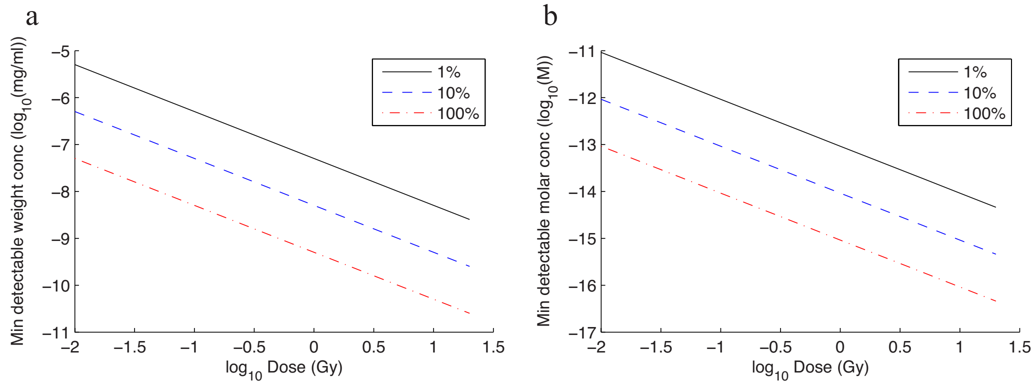

FIG. 4. Minimum estimated phosphor concentrations calculated from the literature and our own data. Lines represent phosphor luminescence efficiencies; the 100% line is based on efficiency data from a $La_2O_2S{:}Tb$ phosphor reported by Kandarakis *et al.* (a) Minimum weight concentration (in mg/ml) vs dose (Gy). (b) Minimum molar concentration (in M) vs dose (Gy).

compare the contrast differences between x-ray fluoroscopy and x-ray/optical luminescence imaging in the small-animal imaging phantom described in Sec. II D. The phantom was imaged during fluoroscopy operation with the tube voltage at 100 kV and the tube current at 10 mA. The x-ray source was placed above the phantom to evenly irradiate the volume. The CCD camera was placed within 15 cm of the phantom and oriented orthogonal to the direction of irradiation. The fluoroscopy image was taken simultaneously. It is important to note that gadolinium is a strong absorber of 100 keV x-ray energy, with a mass attenuation coefficient of 3.109 cm^2/g (compared to common x-ray contrast agents such as barium at 2.196 cm^2/g and iodine at 1.942 cm^2/g). Since gadolinium has a higher mass attenuation coefficient for x-ray photons than water (mass attenuation coefficient of 0.1707 cm^2/g), it should exhibit slight contrast.

The images from the phantom are shown in Fig. 5. Figure 5(a) shows a white light image taken by the CCD camera with background illumination from the room lights. The corresponding fluoroscopy image is shown in Fig. 5(b). The phosphor inclusion is indicated by the red arrow and shows slight increased x-ray absorption (the smaller dark circle is a bolt hole in the aluminum optical table). Figure 5(c) shows a raw optical image taken of the x-ray luminescent phosphor. This image is overlaid on the white light image in Fig. 5(d). The contrast between the inclusion and the background is very slight, at 0.6% for the fluoroscopy image, while it is over 260% for the luminescence image. In addition, the signal-to-noise ratio for the phosphor emission was 23 vs 2.4 for the fluoroscopy image.

AQ: #4

IV. DISCUSSION

We found that dose distributed to the shielded camera was measured at less than 3 $\mu Gy/s$ when the camera was positioned at the isocenter and the x-ray tube voltage was 100 keV with the tube current at 20 mA. Although this dose is low, estimating a damage threshold is difficult for CCDs because damage is design/manufacturer-specific and is dependent on environmental conditions (for a more thorough overview, see Ref. 16). It is well recognized that the largest radiation threat to the operation of a CCD is the bombardment by highly energetic heavy particles, such as protons and neutrons. These particles contribute most to CCD damage through impact displacements of silicon atoms which create semipermanent energy traps. These traps create energy levels which can increase Johnson noise (via promoting valence band electrons to the conduction band), create spurious noise when trapped electrons are released, and alter the operation of transistor gates by altering their flat-band voltage (for a more thorough review, see Refs. 17 and 18). Although the probability of creating protons and neutrons is extremely low at diagnostic x-ray energies studied here, it is relevant for therapeutic energies in the MV range. Cumulative doses are also important because of the increased probability for a high-energy photon interaction. It has been reported that total

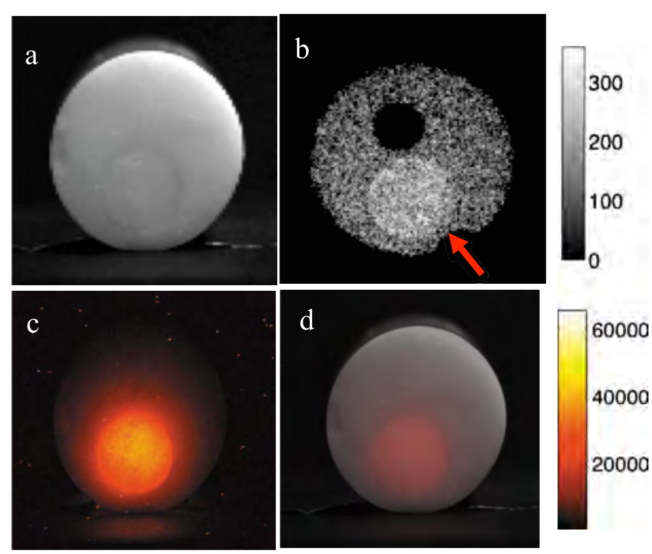

FIG. 5. Agar imaging phantom with embedded phosphors and tissue emulating optical properties. (a) White-light optical image. (b) Projection fluoroscopy image (note the distinction between the phosphor inclusion—indicated by the red arrow—around 300 units, compared to the black circle caused by a screw hole in the optical table supporting the phantom). (c) Optical emission from the phantom. (d) Overlay of the white light image (a) and the light emission (c).

AQ: #12

doses above about 25 and 100 Gy are considered thresholds for increased noise and permanent damage, respectively[19] (though again, these numbers are highly camera-dependent). Thus, it is important to keep radiation dose on the CCD as low as possible to minimize cumulative dose and increase the life of the camera. The dose deposited in this experiment of $1-3\ \mu\text{Gy/s}$ is minimal, and damage due to radiation should be insignificant in the lifetime of the camera.

The lanthanide dopants examined in this study are known to have extremely sharp peaks; for example, we measured the full width at half maximum (FWHM) of the GOS:Tb sample at 3 nm, while the GOS:Eu sample had a FWHM of 2 nm for the largest peak [both shown in Fig. 3(a)]. This is in contrast to common fluorophores like indocyanine green, which have often have emission peak FWHM of about 60 nm. This enables the possibility of multiplexing contrast agents with very little cross-talk, allowing the simultaneous measurement of several markers for disease.

A major concern of these x-ray excitable phosphor contrast agents is that they require ionizing dose to activate. Thus, lower concentrations of phosphors will necessitate higher doses. We analyzed the practical detection limit of phosphors using the knowledge of concentration and dose linearity and luminescence efficiencies found in the literature for similar nanophosphors. For detection at the surface of tissue, x-ray mammographic dose should be sufficient to allow the detection of picomolar (ng/ml) concentrations of phosphor. This finding is corroborated with our experimental results shown in Fig. 3. If the data in Fig. 3(d) are extrapolated to 10 counts/pixel, adequate signal-to-noise ratio is achieved using an EM-CCD camera (with dark noise of 0.05 counts/pixel for this acquisition). Placing the camera within a few cm (compared to 20 cm in this experiment) would result in the detection of approximately two orders of magnitude more light. Further, if the dose is increased by an order of magnitude [from the 4 mGy dose administered for Fig. 3(d)] to mammography levels, and EM gain is increased to the maximum, concentrations of ng/ml (picomolar) may be realized.

At deeper depths, however, light attenuates rapidly; for example, in breast tissue, a depth of 3 cm would attenuate detected light by approximately three orders of magnitude.[20] This would effectively decrease phosphor sensitivity during mammographic dose to nanomolar concentrations. In a radiation oncology setting, however, high doses are delivered to treat disease (such as the 20 Gy single-fraction therapy, which is used during intraoperative radiation therapy[21]). This technique could aid a surgeon and radiation oncologist to identify the distribution of disease around a tumor margin, such as during breast lumpectomy. In this case, the patient would be injected with a phosphor contrast agent before or during surgery, depending on the pharmacokinetics of the tracer. The tracer could be imaged during the first 1% or 10% (e.g., 0.2 or 2 Gy) of the radiotherapy treatment dose, which would provide the clinicians with more confidence about the treatment dose or volume, or enable an adjustment to the dose distribution.

The other area of concern with these particles is biological compatibility. This is an issue for all nanoparticle systems, and much work is being done to develop strategies to ensure stability and compatibility.[22] In fact, multiple groups have successfully used upconversion phosphors in biological small-animal models.[23,24] The increased interest in phosphors should aid in the rapid advancement in biocompatibility, which will aid this modality.

We found that the contrast to background ratio was over 2.5 orders of magnitude higher for optical detection of the luminescent phosphors compared to x-ray fluoroscopy. The actual contrast amplification is much higher since the optical photons emitted from the inclusion exhibit extensive scatter in the background and subsequently are detected by the CCD. These scatter effects would be greatly minimized via modeling of the light propagation. In comparison, x-ray photon scatter is relatively nonexistent so that the signal contribution from the background originating from the inclusion is negligible. Considering the photon scatter should greatly improve the contrast of these phosphors for optical detection compared to fluoroscopy.

Although this work demonstrated the potential of x-ray luminescence imaging for imaging a superficial object, imaging of lesions centimeter deep should be possible, with contrast-resolution limitations depending on tissues' properties, concentration, and nonspecific uptake. The development of deep-tissue x-ray luminescence imaging will require the incorporation of optical tomographic models. With x-ray luminescent imaging, the x-ray source must be modeled in tissue to give an accurate description of dose. There are many sophisticated tools to model dose, such as Monte Carlo or analytical models, which have been shown to be accurate [e.g., within 4% (Ref. 25)] in biological tissues. Concurrent x-ray structural imaging will further improve these calculations. After dose distribution is calculated, tomographic imaging may be performed with a reconstruction model that uses a model of the light propagation in tissue to minimize the difference between calculated and optical measurements. This is very similar to the fluorescence molecular imaging problem.[26] Once again, the knowledge of anatomical information will aid the optical reconstruction problem by providing structural detail which may be used to improve optical modeling[27] and reconstruction.[28]

The joint use of x-ray activated phosphors for molecular imaging offers several advantages to x-ray imaging and to all-optical fluorescent imaging. For x-ray imaging, contrast agent imaging is currently limited to high concentrations of nonspecific iodine or barium sulfate. Optimal concentrations for these contrasts have been reported around 300–500 mg/ml.[29] These high concentrations are impractical for imaging biological targets.[2] The ability to image cellular targets would be a great benefit to x-ray imaging, which, despite being the most prominent modality in use in the clinic today, is generally limited to imaging structural anatomy. The use of phosphors combined with the sensitivity of optical imaging allows lower, more biologically feasible concentrations of contrast agents than is currently available with x-ray imaging alone.

The use of x-ray activated phosphors offers three unique advantages to all-optical approaches. First, this dual-modality instrument offers inherent spatial coregistration between anatomical features and optical contrasts. This registration is critical for imaging functional pathology in deep tissue [hence, the need for positron emission tomography (PET)/CT imaging systems].[30] Next, the use of x-ray excitation eliminates the optical autofluorescence issue in optical imaging. Since the x-ray excitation spectrum is undetectable with photo-optical detectors, autofluorescence is avoided, which potentially reduces the detection limit for low concentrations. Finally, this technique is also expected to have increased depth performance over optical imaging, because of the high penetration of x-ray photons in tissues. X-ray photons have nearly two orders of magnitude lower effective attenuation coefficient compared to optical photons; this opportunity offers the potential to use clinically available instrumentation as an external source.

V. CONCLUSIONS

This study focused on the instrumentation and material feasibility of inorganic downconversion phosphors toward the realization of x-ray molecular imaging. Significant recent advances in PET,[4] optical imaging,[11] magnetic resonance imaging,[12] and to a lesser extent, single positron emission computed tomography, and ultrasound have invigorated the search for disease-specific protein receptors that may be targeted with imaging agents. This approach has already been applied to numerous pathologies to identify atherosclerosis and thrombosis,[31] to determine treatment efficacy via apoptosis markers,[32] to identify cancer, and to monitor cellular activity. The incorporation of these markers into x-ray imaging may have significant impact on medical imaging.

In this work, we demonstrate, for the first time to our knowledge, the feasibility of using inorganic phosphors to enable optical detection under x-ray irradiation, which may enable x-ray molecular imaging. We first investigated the practical feasibility of operating a CCD within an x-ray excitation field at clinically relevant energies, taking into consideration noise and potential damage. We found that the dose distribution to air was sufficiently low to prevent damage during operation. Additionally, the noise on the CCD due to incoming high-energy irradiation is manageable. We demonstrated the ability of several phosphors to emit light in the optical regime under x-ray excitation. These phosphors should be effective for tuning light output to a specific application. We found that the light output was linearly proportional to both dose and concentration. Future work will focus on quantitative imaging. We calculated minimum detectable concentrations based on these data and values found in literature; these concentrations are sufficient for certain biological imaging applications. Finally, we demonstrated the potential of inorganic phosphors to image lower concentrations than is possible with x ray alone. We found a 430 times improvement in contrast recovery for optical detection compared to fluoroscopic detection. This improvement is expected to be greater with modeling of photon propagation and imaging. We envision hybrid x-ray/optical imaging may have significant application in the detection and diagnosis of disease, especially during image-guided intervention.

ACKNOWLEDGMENTS

The authors would like to thank Dr. Catherine Klifa from the University of California, San Francisco for the use of the diffuse optical spectroscopy system. They gratefully acknowledge funding sources from the NSF (Grant No. 0854492), NIH (Grant No. R01 CA133474), and NCI ICMIC (Grant No. P50 CA114747).

[a]Electronic mail: colincarpenter@stanford.edu
[1]F. A. Jaffer and R. Weissleder, "Molecular imaging in the clinical arena," JAMA, J. Am. Med. Assoc. **293**(7), 855–862 (2005).
[2]U. Speck, "Contrast agents: X-ray contrast agents and molecular imaging—A contradiction?," Handb Exp Pharmacol **185**, 167–175 (2008).
[3]R. Weissleder and M. J. Pittet, "Imaging in the era of molecular oncology," Nature (London) **452**(7187), 580–589 (2008).
[4]S. S. Gambhir, "Molecular imaging of cancer with positron emission tomography," Nat. Rev. Cancer **2**(9), 683–693 (2002).
[5]J. Bushberg, J. Seibert, E. Leidholdt, and J. Boone, *The Essential Physics of Medical Imaging*, 2nd ed. (Lippincott Williams & Wilkins, Philadelphia, 2002).
[6]W. M. Yen and M. J. Weber, *Inorganic Phosphors: Compositions, Preparation and Optical Properties* (CRC, Boca Raton, FL, 2004)
[7]H. Chander, "Development of nanophosphors—A review," Mater. Sci. Eng. R. **49**(5), 113–155 (2005).
[8]I. Kandarakis, D. Cavouras, G. Panayiotakis, T. Agelis, C. Nomicos, and G. Giakoumakis, "X-ray induced luminescence and spatial resolution of La2O2S:Tb phosphor screens," Phys. Med. Biol. **41**(2), 297–307 (1996).
[9]Y. Jiang, Y. Wu, Y. Xie, and Y. Qian, "Synthesis and characterization of nanocrystalline lanthanide oxysulfide via a La(OH)(3) gel solvothermal route," J. Am. Ceram. Soc. **83**(10), 2628–2630 (2000).
[10]D. Cavouras, I. Kandarakis, T. Maris, G. S. Panayiotakis, and C. D. Nomicos, "Assessment of the gain transfer function of phosphors for application in medical imaging radiation detectors," Eur. J. Radiol. **35**(1), 70–77 (2000).
[11]B. W. Pogue and M. S. Patterson, "Review of tissue simulating phantoms for optical spectroscopy, imaging and dosimetry," J. Biomed. Opt. **11**(4), ■–■ (2006).
[12]T. Pham, O. Coquoz, J. Fishkin, E. Anderson, and B. Tromberg, "Broad bandwidth frequency domain instrument for quantitative tissue optical spectroscopy," Rev. Sci. Instrum. **71**(6), 2500–2513 (2000).
[13]C. W. E. van Eijk, "Radiation detector developments in medical applications: Inorganic scintillators in positron emission tomography," Radiat. Prot. Dosim. **129**(1–3), 13–21 (2008).
[14]W. Chen and J. Zhang, "Using nanoparticles to enable simultaneous radiation and photodynamic therapies for cancer treatment," J. Nanosci. Nanotechnol. **6**(4), 1159–1166 (2006).
[15]J. A. Parrish, "New concepts in therapeutic photomedicine: Photochemistry, optical targeting and the therapeutic window," J. Invest. Dermatol. **77**(1), 45–50 (1981).
[16]J. Pickel, A. Kalma, G. Hopkinson, and C. Marshall, "Radiation effects on photonic imagers—A historical perspective," IEEE Trans. Nucl. Sci. **50**(3), 671–688 (2003).
[17]D. Neamen, *Semiconductor Physics and Devices* (McGraw-Hill, New York, 2002).
[18]G. Hopkinson, C. Dale, and P. Marshall, "Proton effects in CCDs," IEEE Trans. Nucl. Sci. **43**(2), 614–627 (1996).
[19]C. Marshall and P. Marshall, "CCD radiation effects and test issues for satellite designers," NASA Electronic Parts and Packaging (2003), p. 1053.
[20]D. A. Boas, D. H. Brooks, E. L. Miller, C. A. DiMarzio, M. Kilmer, R. J. Gaudette, and Q. Zhang, "Imaging the body with diffuse optical tomography," IEEE Signal Process. Mag. **18**, 57–75 (2001).
[21]U. Veronesi, G. Gatti, A. Luini, M. Intra, R. Orecchia, P. Borgen, M. Zelefsky, B. McCormick, and V. Sacchini, "Intraoperative radiation

therapy for breast cancer: Technical notes," Breast J. **9**(2), 106–112 (2003).

[22] I. Brigger, C. Dubernet, and P. Couvreur, "Nanoparticles in cancer therapy and diagnosis," Adv. Drug Delivery Rev. **54**(5), 631–651 (2002).

[23] J. Shen, L. Sun, and C. Yan, "Luminescent rare earth nanomaterials for bioprobe applications," Dalton Trans. ■, 5687–5697 (2008).

[24] C. Vinegoni, D. Razansky, S. A. Hilderbrand, F. Shao, V. Ntziachristos, and R. Weissleder, "Transillumination fluorescence imaging in mice using biocompatible upconverting nanoparticles," Opt. Lett. **34**(17), 2566–2568 (2009).

[25] E. S. M. Ali and D. W. O. Rogers, "Benchmarking EGSnrc in the kilovoltage energy range against experimental measurements of charged particle backscatter coefficients," Phys. Med. Biol. **53**(6), 1527–1543 (2008).

[26] S. C. Davis, B. W. Pogue, H. Dehghani, and K. D. Paulsen, "Contrast-detail analysis characterizes diffuse optical fluorescence tomography image reconstruction," J. Biomed. Opt. **10**(5), 050501 (2005).

[27] D. Hyde, R. Schulz, D. Brooks, E. Miller, and V. Ntziachristos, "Performance dependence of hybrid x-ray computed tomography/fluorescence molecular tomography on the optical forward problem," J. Opt. Soc. Am. A Opt. Image Sci. Vis **26**(4), 919–923 (2009).

[28] A. Li, E. L. Miller, M. E. Kilmer, T. J. Brukilaccio, T. Chaves, J. Stott, Q. Zhang, T. Wu, M. Choriton, R. H. Moore, D. B. Kopans, and D. A. Boas, "Tomographic optical breast imaging guided by three-dimensional mammography," Appl. Opt. **42**(25), 5181–5190 (2003).

[29] Z. Szucs-Farkas, F. R. Verdun, G. von Allmen, R. L. Mini, and P. Vock, "Effect of x-ray tube parameters, iodine concentration, and patient size on image quality in pulmonary computed tomography angiography: A chest-phantom-study," Invest. Radiol. **43**(6), 374–381 (2008).

[30] D. W. Townsend, "Multimodality imaging of structure and function," Phys. Med. Biol. **53**(4), R1–R39 (2008).

[31] R. Weissleder and V. Ntziachristos, "Shedding light onto live molecular targets," Nat. Med. **9**(1), 123–128 (2003).

[32] F. G. Blankenberg, "In vivo detection of apoptosis," J. Nucl. Med. **49**, 81S–95S (2008).

TB, RML, US, PMB/379620, 29/04/2011

IOP PUBLISHING PHYSICS IN MEDICINE AND BIOLOGY

Phys. Med. Biol. **56** (2011) 1–16 UNCORRECTED PROOF

Limited-angle x-ray luminescence tomography: methodology and feasibility study

C M Carpenter, G Pratx, C Sun and L Xing

Department of Radiation Oncology, School of Medicine, Stanford University, Stanford, CA 94305, USA

E-mail: colincarpenter@stanford.edu

Received 26 December 2010, in final form 23 March 2011
Published DD MMM 2011
Online at stacks.iop.org/PMB/56/1

Abstract

X-ray luminescence tomography (XLT) has recently been proposed as a new imaging modality for biological imaging applications. This modality utilizes phosphor nanoparticles which luminesce near-infrared light when excited by x-ray photons. The advantages of this modality are that it uniquely combines high sensitivity of radioluminescent nanoparticles and high spatial localization of collimated x-ray beams. Currently, XLT has been demonstrated using x-ray spatial encoding to resolve the imaging volume. However, there are applications where the x-ray excitation may be limited by geometry, where increased temporal resolution is desired, or where a lower dose is mandatory. This paper extends the utility of XLT to meet these requirements by incorporating a photon propagation model into the reconstruction algorithm to recover dimensions remaining in an x-ray limited-angle (LA) geometry. This enables such applications as image-guided surgery, where the ability to resolve lesions at depths of several centimeters can be the key to successful resection. The hybrid x-ray/diffuse optical model is first formulated and then demonstrated in a breast-sized phantom, simulating a breast lumpectomy geometry. Both numerical and experimental phantoms are tested, with lesion-simulating objects of various sizes and depths. Results show localization accuracy with median error of 2.2 mm, or 4% of object depth, for small 2–14 mm diameter lesions positioned from 1 to 4.5 cm in depth. This compares favorably with fluorescence optical imaging, which is not able to resolve such small objects at this depth. The recovered lesion size has lower size bias in the x-ray excitation direction than the optical direction, which is expected due to the increased optical scatter. However, the technique is shown to be quite invariant in recovered size with respect to depth, as the standard deviation is less than 2.5 mm. Sensitivity is a function of dose; radiological doses are found to provide sufficient recovery for μg ml^{-1} concentrations, while therapy dosages provide recovery for ng ml^{-1} concentrations. Experimental phantom results agree closely with the numerical results, with positional errors recovered within

8.6% of the effective depth for a 5 mm object, and within 5.2% of the depth for a 10 mm object. Object-size median error is within 2.3% and 2% for the 5 and 10 mm objects, respectively. For shallow-to-medium depth applications where optical and radio-emission imaging modalities are not ideal, such as in intra-operative procedures, LAXLT may be a useful tool to detect molecular signatures of disease.

(Some figures in this article are in colour only in the electronic version) **Q1**

1. Introduction

Imaging plays a vital role in the management of cancer care, for detection, staging, intervention, and monitoring of treatment response. Despite its ubiquitous use elsewhere, the role of imaging in surgery is limited, as it is dominated by C-arm fluoroscopy and optical endoscopy. These tools are appropriate for visualizing tissue structure, yet are limited in their sensitivity to microscopic disease. This limitation affects such procedures as surgical breast lumpectomy, as many studies have found that surgeons are unable to remove all tumor tissue present in the surgical field (for example, Gibson *et al* (2001) identified residual tumor in 55% of the cases. The risks of local failure are high, as local failure often leads to distant metastasis (Fortin *et al* 1999). Thus, there is a need for tools to provide surgeons with more sensitive, more specific image guidance.

This need may be fulfilled with molecular imaging, which promises to image molecular and cellular processes, and may allow the early identification of disease or status of disease progression and treatment (Weissleder and Pittet 2008). Developing these tools for the operating room would aid a physician during an intervention, by allowing the clinician to identify near-microscopic regions of disease, such as at the tumor margin. Ideally, this tool would be able to image at a depth of several centimeters, so that disease buried beneath the superficial layers could be identified. Several potential applications for this technology could be in removing occult disease in breast (Tanaka *et al* 2006, Alex and Krag 1993), brain (Stummer *et al* 2008) and hepatic tumors (Torzilli *et al* 1999), where imaging is currently being incorporated into the clinic, and new innovations may be readily translated.

This paper develops and demonstrates a novel x-ray luminescence tomographic (XLT) method that is uniquely suited for image-guided surgical applications. This method, Limited-Angle XLT (LAXLT), utilizes a photon propagation model to enable XLT for surgical guidance, where XLT's advantages are the clearest for translation into the clinic. XLT has been recently introduced (Carpenter *et al* 2010) and demonstrated in simulation and in phantoms (Pratx *et al* 2010a, 2010b). This imaging modality utilizes nano-sized phosphors which emit optical near-infrared light upon x-ray excitation (Chen 2008, Sun *et al* 2010). Attaching these phosphors to molecular probes (e.g. antibodies and peptides) that target molecular markers specific to tumors, such as angiogenesis markers like epidermal growth factor receptor (Sokolov *et al* 2003), or $\alpha_v\beta_3$-integrin (Haubner *et al* 2001, Chen *et al* 2004) expression, could allow the surgeon to differentiate between normal and cancerous tissue. XLT has several advantages to current molecular-sensitive imaging modalities: emission imaging techniques, such as gamma cameras, are limited in their ability to discriminate depth due to the limited angles that may be imaged during surgical procedures (Barrett 1990); optical imaging, on the other hand, has the ability to provide depth localization, and is currently under investigation for surgical guidance (Tanaka *et al* 2006, Stummer *et al* 2008, Roberts *et al* 2010), yet is limited in its ability to

image deeper than ∼1 cm (Kepshire *et al* 2007). Depth is important to discern to determine occult lesions lying under the superficial layer, and to determine the feasibility of surgical removal of a lesion.

XLT utilizes the extremely low scatter of x-rays compared to optical fluorescence imaging to enable higher spatial resolution. A thin pencil-beam of collimated x-rays may be maintained while the x-rays propagate through tissue of several cm; this spatial localization is in contrast to optical excitation, which is highly attenuated and scattered (O'Leary *et al* 1995). By rotating the x-ray (or similarly the phantom) to cover all angular projections, the resolving power is limited merely by the width of the beam (up to the diffraction of the x-ray). A numerical analysis demonstrated that 2.25 cm deep objects as small as 1 mm (using a 1 mm beam width) with a nanoparticle concentration of 0.4 pM could be resolved; increasing dose increased the sensitivity (Pratx *et al* 2010a). However, there are applications where the x-ray excitation may be limited by geometry, where increased temporal resolution is desired, or where a lower dose is mandatory; one such application is intraoperative breast cancer lumpectomy, where it may not be possible or desirable to irradiate over the full projection space. In these cases, it would be beneficial to irradiate over a limited projection space, and use the ability of the optical detectors to resolve the remaining dimensions. This technique could also have utility in decreasing dose to the tissue, as fewer irradiation beamlets are needed to resolve the volume.

This paper develops a reconstruction methodology for utilizing XLT to perform depth-resolved imaging in a geometry appropriate for tumor-resection applications. This method develops a hybrid x-ray/optical reconstruction, which allows XLT spatial encoding in a limited-angle geometry, and diffuse optical spatial discrimination for the remaining dimensions. This technique augments that of Pratx *et al* (2010a), who encoded all spatial dimensions; such a technique is more suitable for such applications as small-animal imaging. The advantage of this new approach is that enables XLT in surgical applications such as breast or brain excision, and may reduce dose. The performance of this technique is examined in both numerical and experimental phantoms for various object sizes and positions, within a geometry that mimics breast and brain intraoperative geometries.

2. Methods

2.1. Experimental setup

The equipment used for this study consisted of an x-ray radiation source to excite the phosphors, and an optical detector to sample the photon fluence. During acquisition, the radiation source is collimated into a thin slice as described by Pratx *et al* (2010a) to excite a plane shaped volume. An optical camera samples the emitted light. This schematic is shown in figure 1(a). The experimental setup is shown in figure 1(b).

The x-ray source used for the measurements in this paper was a 50 kVp x-ray superficial unit (Pantak Therapax-150, Elimpex, AT) with a 10 cm exit-diameter cone applicator. This cone was placed 17.5 cm away from surface of the phantom. The beam was collimated to 1 mm wide (verified optically) by carefully positioned 50 mm thick lead bricks. A high-sensitivity EM-CCD camera (Pro-EM, Princeton Instruments, NJ) with an F/1.4 lens was positioned ∼20 cm away from the surface of the phantom. This distance was chosen to minimize x-ray photon noise (Carpenter *et al* 2010). As an alternative, optically clear leaded acrylic or leaded glass could be placed between the camera and the sample and used to reduce x-ray noise on the CCD and allow the camera to be placed closer to the sample to collect more light.

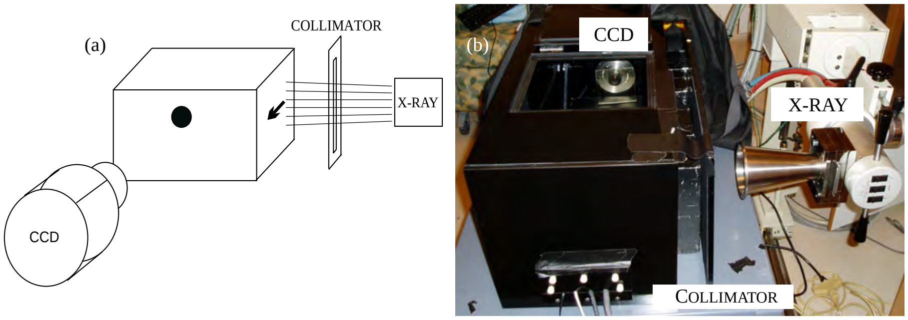

Figure 1. (a) Schematic of LAXLT while imaging a phantom with a single spherical object. (b) Experimental setup used in this study. A black-box was used to enclose the phantom (not shown) and eliminate ambient light from the experiment.

2.2. Image formation

2.2.1. X-ray luminescence emission forward model. To determine the concentration of nanophosphors, the radiation (x-ray and optical) must be modeled. The emission of x-ray excitable nanophosphors is linearly dependent on the dose imparted to the tissue (Carpenter *et al* 2010), d (units of Gy), the fractional efficiency of the phosphor in converting ionizing energy to optical emission, Γ, and the concentration, c (units of mg ml^{-1}). The luminescent photon density from the nanophosphors, Φ, due to an incident radiation beam is therefore

$$\Phi = \Gamma d c. \tag{1}$$

Determining the total ionization energy imparted to the tissue (dose) is a procedure that requires calibration to incorporate the properties of the radiation emitted by the x-ray system. This calibration is system specific, taking into account tube potential, geometry, x-ray tube target, and filter material; these factors taken together form an x-ray spectrum, known as the beam quality. The dose at depth is determined using measurements from a calibrated ionization chamber in a phantom and composed into a look-up table, the percent depth dose (PDD) curves. This system-wide calibration is performed periodically (Ma *et al* 2001). Using the PDD curves, dose at a specific depth in the tissue can be determined by knowing the source-to-surface distance between the x-ray tube and the tissue. This method can have high quantitative accuracy of 1–2% (Munck af Rosenschöld *et al* 2008). Another method to accurately determine dose is through Monte Carlo methods, which model the system, including the above factors and also including patient anatomy. This method can calculate dose with high accuracy as long as comprehensive modeling of beam quality is performed (Verhaegen *et al* 1999). In this study, we used the PDD curves to determine dose.

2.2.2. Diffuse optical forward model. Images acquired at the tissue surface are input into a photon propagation model to determine the phosphor distribution. The images from the CCD camera are first processed to remove x-ray noise using a simple gradient-threshold algorithm, and then input into the algorithm as the data. The propagation of optical light can be approximated by the lossy photon diffusion equation (DE) (Arridge *et al* 1993), which yields the photon density in tissue. The DE is valid for many soft human tissues, including the breast, lung, prostate, brain, etc (Cheong *et al* 1990). Following excitation from x-ray

radiation, the time-independent luminescence photon density emitted from the nanophosphors is

$$\Phi(r) = -\nabla \cdot D(r)\nabla\phi(r) + \mu_a(r)\phi(r) \tag{2}$$

where $\phi(r)$ is the photon fluence at position r, in units of photons per area per time, and $\Phi(r)$ is the photon density, in units of photons per volume per time. Photon propagation is affected by the absorption and diffusion coefficients of the tissue, μ_a and D, respectively, which are dependent on wavelength. The diffusion coefficient, D, is defined as $D = \frac{1}{3(\mu_a+\mu_s')}$, where μ_s' is the reduced scattering coefficient of the emitted photons. A type III boundary condition is used to model the photon fluence at the boundary, $-D\nabla\phi \cdot \hat{n} = \alpha\phi$, where α defines the internal reflection of the light at the tissue boundary due to the index of refraction mismatch between tissue and air (Schweiger *et al* 1995, Aronson 1995), and the unit vector n is normal to the surface of the phantom. Because no unique solution exists for (2) with arbitrary boundaries, equation (2) is approximated with the finite element method (FEM) (Arridge *et al* 1993). This problem is similar to the diffuse optical fluorescence model introduced by Jiang (1998), and is adapted here.

As described by Jiang, the photon emission may be approximated with the FEM by

$$[A]\{\phi\} = \{b\} \tag{3}$$

where A is the FEM approximation of the physics of photon propagation (the right-hand side of equation (2)) and b is the approximation to the light source (the left-hand side of equation (2)). More specifically, the physics of the photon propagation is approximated with the FEM by

$$A_{i,j} = \langle -D\nabla\psi_j \cdot \nabla\psi_i - \mu_a\psi_j\psi_i\rangle \tag{4}$$

where $\psi_{i,j}$ are the volume elements that discretize the imaging domain and form a geometrical mesh defined over the entire imaging domain. A is integrated over this imaging domain. The source (in this case, the light emitted from the phosphors which were excited by the x-ray source) and boundary integral are approximated with the FEM by

$$b_i = -\left\langle \sum_{j=1}^{N} \Phi_j\psi_j\psi_i \right\rangle + \alpha \sum_{j=1}^{M} \phi_j \oint_{\text{boundary}} \psi_j\psi_i \,\mathrm{d}s. \tag{5}$$

The time component of the luminescence lifetime is ignored since the measurements in this work are from an integrating CCD camera, and the measurement time is much greater than the luminescence lifetime; effects from the minimal afterglow of the phosphors are ignored.

The FEM model, G, is used to generate estimates for the photon fluence given the optical properties of the tissue, the concentration of phosphors, c, and the FEM mesh. An estimate for the photon fluence, ϕ, can be calculated by solving equation (3):

$$\phi = G = [A]^{-1}\{b\}. \tag{6}$$

In this paper, the imaging domain is known, and is assumed that the endogenous optical tissue properties are known, so the model is dependent only on the unknown, c. Figure 2 shows the optical photon fluence for a numerical phantom with 100:1 phosphor concentration between an object and the background. Two different source configurations are shown, each with the x-ray direction of propagation in the horizontal (left/right) direction. In figures 2(a) and (b), the x-ray source, indicated by the red circle, irradiates a horizontal line passing through the background, whereas in figures 2(c) and (d), the x-ray irradiates the horizontal line passing through the middle of the phosphor-containing object.

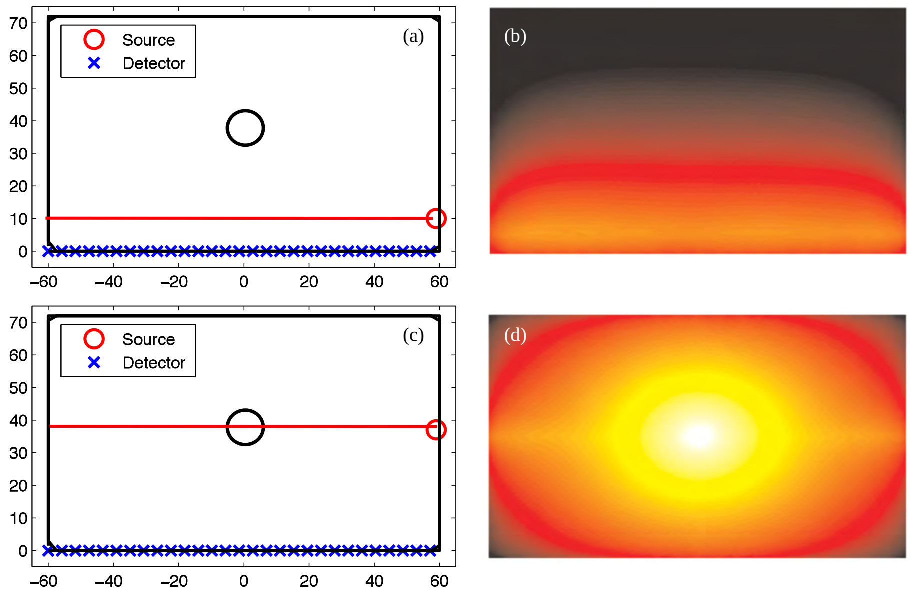

Figure 2. (a) Numerical phantom with a single object located at the center of the domain, and a 10:1 contrast in phosphor between the object and background. The x-ray source irradiates the domain along the long-axis of the phantom at a position of $X = 10$, $Y = -60{:}60$. (b) The emission fluence field of (a). (c) Numerical phantom with the x-ray source irradiating at a position of $X = 40$, $Y = -60{:}60$. (d) The emission fluence field of (c).

2.2.3. X-ray nanophosphor concentration reconstruction. The goal of XLT is to determine the phosphor distribution. This spatial distribution can be determined by minimizing the difference between the measured photon flux from the camera, $\phi_M(r)$, and the simulated photon flux, $\phi_S(r)$ at identical sample locations. This is accomplished by minimizing the L2-norm of the objective function in an optimization routine:

$$\Omega = (\phi_S - \phi_M)^2 \tag{7}$$

where Ω is the objective function to minimize. Because of the large dynamic range, the first term in (7) is formulated from the natural logs of the photon fluxes. This is an underdetermined problem, as measurements are made only at the boundary. Because this problem is underdetermined, the model, G, is linearized with a Taylor approximation and formed into an iterative algorithm as

$$G(c_i) = G(c_{i-1}) + G'\Delta c \tag{8}$$

where G' is the partial differential of the model with respect to the concentration, also known as the Jacobian, J. Minimizing equation (7) with respect to c and substituting $G(c_i)$ from equation (8) into ϕ_S and J for G' yields

$$2J((G(c_{i-1}) + J\Delta c) - \phi_M) = 0 \tag{9}$$

Solving for the concentration yields

$$\Delta c = -[J^T J]^{-1} J^T (\phi_S - \phi_M)$$

This problem is ill-posed, so it is solved using the Levenberg–Marquardt (1963) algorithm, which includes a stabilization parameter, λ, in the inversion to avoid singularities:

$$\Delta c = -[J^T J + \lambda I]^{-1} J^T (\phi_S - \phi_M). \tag{10}$$

Equation (5) is iterated until a minima is reached (the L2 norm of the update is less than 1% of the previous iteration), or until 15 iterations are performed, whichever occurs earlier. The stabilization parameter is reduced at each iteration as the algorithm approaches the minimum and converges on the solution.

Although this study focused on applications where a single angle is ideal, note that this algorithm is not limited to a single angle. Thus, this algorithm is appropriate for any sparse-angle geometry.

2.3. Phantom study

The performance of the experimental setup and the reconstruction algorithm were tested by varying the size and location of a lesion-simulating object. The relationships between source–object and detector–object distance on resolving an object of various sizes were determined with both numerical and experimental phantoms. The metrics used to determine system performance were object location and object size. Location error in both the x-ray excitation and optical read-out dimensions was determined by calculating the distance between the true centroid of the lesion and the location of the maximum recovered value of the phantom. Object size in both the x-ray excitation and optical read-out dimensions were determined by calculating the full width at half maximum (FWHM) of the object in these dimensions. Concentration sensitivity and contrast recovery were also examined.

2.3.1. Numerical phantoms. Numerical phantoms were utilized to test the position accuracy, object-size accuracy, and sensitivity of the algorithms. The position and object-size phantoms investigated the recovery of simulated tumors with 10:1 contrast between the object and the background and phosphor concentrations of 10 μg ml^{-1}. These lesions varied in size between 2 and 14 mm, and were placed at different locations in the phantom, as depicted in figures 3(a) and 4(a) (note the multiple arrows, which indicate the minimum and maximum extent of the object locations investigated). Sufficient dose (1 cGy) was given to yield signal-to-noise (SNR) greater than 10 for each object position—this methodology allowed a performance test of the algorithm for all object positions.

The sensitivity phantom included an object with varying concentration (figure 5(a)), and varying contrast (figure 5(b)). The 6 mm diameter object was placed at the center of the phantom along the dimension of the detectors (the long-axis), and moved at various depths away from the detectors. We used the phosphor properties from Kandarakis *et al* (1996) to obtain quantification of the emitted light efficiency for their lanthanum oxysulfide:terbium phosphor, which was 1.39 $\times$ 10^{15} optical photons/(Gy $\times$ mg). We incorporated solid-angle losses as well as losses due to lens inefficiency (DO-1795, Navitar Imaging Solutions, Rochester, NY). SNR below 10 was assumed to be too low to detect.

All phantoms were two dimensional, and measured 12 cm $\times$ 6 cm. Detectors were placed along the long-axis of the phantom, while the collimated x-ray source, 1 mm wide, was scanned along the short axis. The phosphor used for this experiment mimicked GOS:Eu, demonstrated in x-ray luminescence imaging in a previous study, which has a strong luminescence emission at ~618 nm. Background optical properties were similar to that of breast tissue (Peters *et al* 1990) ($\mu_a = 0.0027$, $\mu_s' = 0.717$).

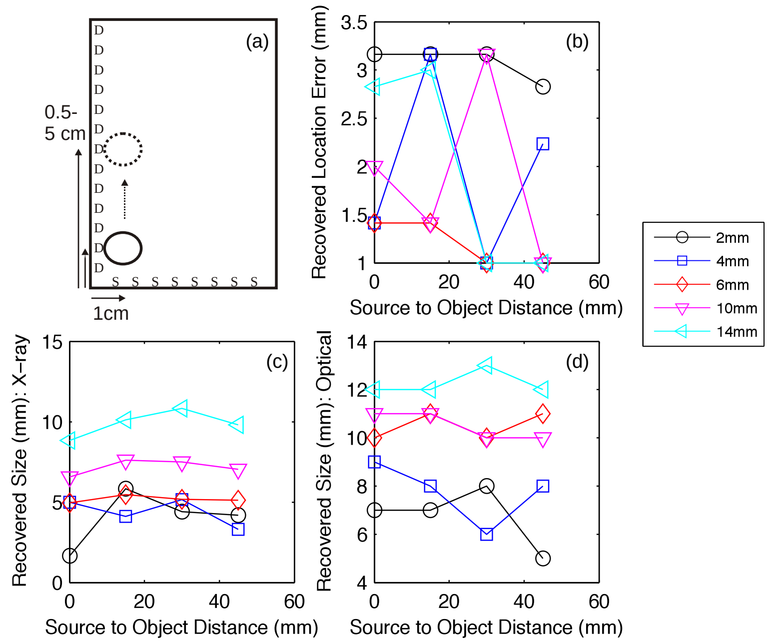

Figure 3. (a) Numerical phantom experiment examining the effect of moving a variable-sized object away (four positions, indicated by the arrows) from the x-ray source plane (S), while keeping the distance from the detection plane (D) fixed. (b) Recovered object location error. (c) Recovered object diameter FWHM with respect to the x-ray source dimension. (d) Recovered object diameter FWHM with respect to the optical detection dimension.

2.3.2. Experimental phantom. The experimental phantom is shown in figure 6. Figures 6(a) and (b) show the relative layout of the objects in the phantom, while figure 6(c) shows the camera-eye view of the phantom. Figure 6(d) shows an image of the phantom while the phantom is irradiated by the x-ray beam. The optically clear acrylic phantom, measuring 12 cm $\times$ 6 cm, was filled with India ink to mimic optical absorption, and intralipid to mimic optical scatter, at the appropriate concentrations. The optical properties were $\mu_a = 0.0027$ and $\mu_s' = 0.717$, as determined from a diffuse optical spectroscopy system. GOS:Eu phosphor at a concentration of 10 mg ml^{-1} was added to two cylindrical inclusions, one 5 mm in diameter, and one 10 mm in diameter, which were located 3 and 9 cm from the edge nearest the x-ray source, respectively. The inclusions were both imaged at various depths from the edge nearest the detector: 10, 15, 20, 30 mm; these dimensions are shown more clearly in figure 7(a). The exposure times and gains were 1.5 s at gain 500, 3.5 s at gain 800, 3 s at gain 1000, and 7.5 s at gain 1000, for increasing depth. Dose to the phantom varied depending on the phosphor depth, so that a high SNR could be acquired while the phosphors were irradiated. The doses to the phantom were 6.7, 15.6, 13.4, and 33.4 cGy, for increasing depth.

3. Results

3.1. Numerical phantom results

As described above, a lesion-simulating object was placed in various locations in the volume so that the performance of LAXLT could be analyzed. The lesion location was varied with

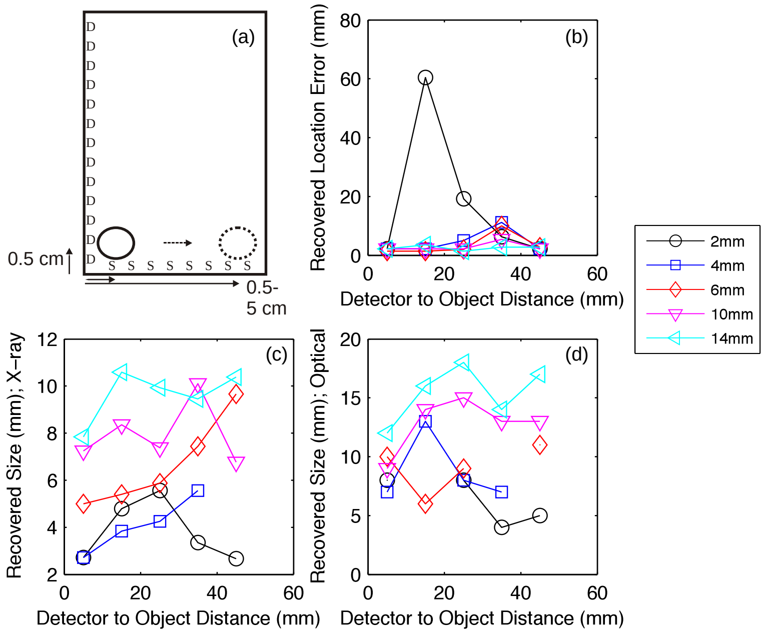

Figure 4. (a) Numerical phantom experiment examining the effect of moving a variable-sized object away (eight positions, indicated by the arrows) from the optical detection plane (D), while keeping the distance from the x-ray source plane (S) fixed. (b) Recovered object location error. (c) Recovered object diameter FWHM with respect to the x-ray source dimension. (d) Recovered object diameter FWHM with respect to the optical detection dimension.

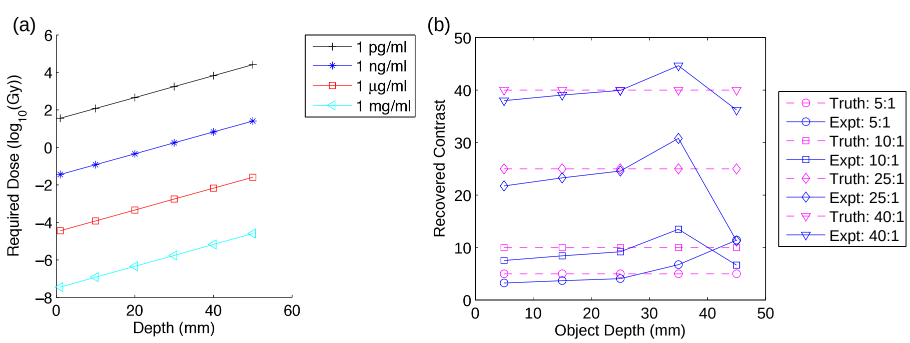

Figure 5. (a) Numerical phantom experiment examining the effect of: (a) variable object to background contrast and (b) variable concentration, of a 6 mm diameter object versus depth from the detection plane.

respect to the source-axis and detection-axis separately to determine the effects of source–object distance and detector–object distance on the ability to resolve the object. Figure 3 shows the results of maintaining a fixed detector–object distance while varying the source–object distance (varying depth with respect to the x-ray). These dimensions are depicted in figure 3(a). The location error for the 2–14 mm objects is shown in figure 3(b). This result

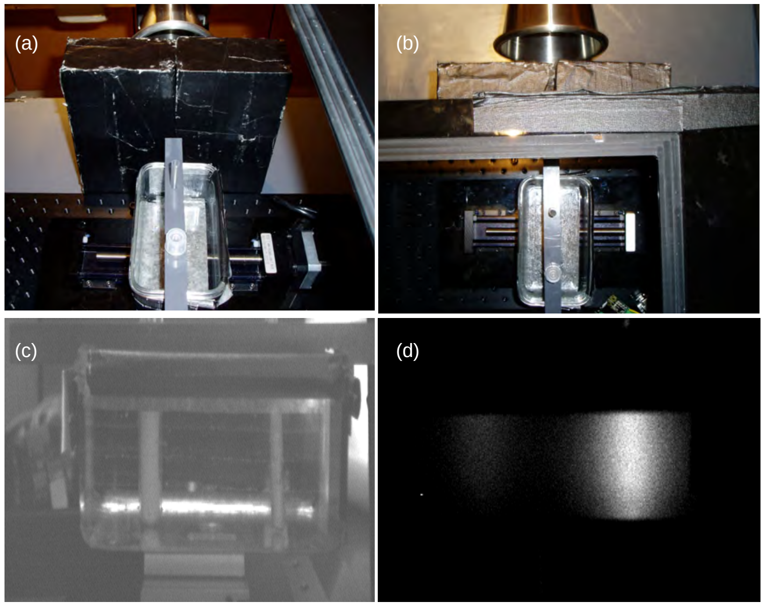

Figure 6. Experimental phantom: (a) and (b) two views from above the black-box including the phantom and collimator bricks. (c) Image taken by the high-sensitivity CCD camera of the phantom under ambient light and no irradiation, (d) CCD image with no ambient light and x-ray irradiation.

demonstrates the excellent ability of the algorithm to spatially resolve an object, as all errors in distance are lower than 3.5 mm. Figure 3(c) shows the recovered object size in the direction of the x-ray excitation, which demonstrates the insensitivity with respect to depth, with an average standard deviation in the error in recovered size of 0.82 mm for varying source–object distances. In figure 3(d), the recovered size of the object in the optical dimension is examined as a function of source–object depth. The algorithm is able to distinguish the varying sizes of the objects, with a standard deviation in the error in recovered size of 0.83 mm for the varying source–object distance. There is a slight tendency for blurring in the optical dimension due to the scattering of the optical photons.

Figure 4 shows the effects of varying the depth of an object with respect to the optical dimension. Figure 4(a) shows the physical dimensions of the phantom. The object was moved from 0.5 to 4.5 cm from the detector, while remaining at a fixed distance from the x-ray source. Figure 4(b) shows the recovered location error of the centroid of the object with respect to depth from the optical detector. In this experiment, the ability to resolve an object of $\sim$2 mm was at the limit of the system with the 1 mm collimated x-ray beam that was used. However, the objects sized 4 mm and larger were resolved with higher accuracy. As expected, location error increases slightly as the depth increases, and larger objects are resolved more accurately than smaller objects. The advantage of using the x-ray is highlighted here, as even at 4.5 cm in depth, the object is resolved with less than 1 cm total error. Figure 4(c) shows the recovery of object size in the x-ray dimension, similar to figure 3(c). The mean standard deviation for the error in recovered object size was 1.36 mm. Figure 4(d) shows that the ability to determine the size of the object in the optical dimension has increased variability compared to the x-ray

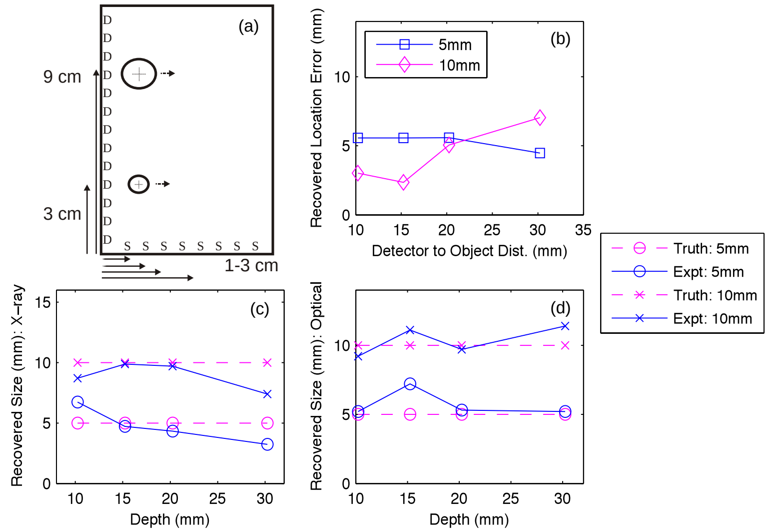

Figure 7. (a) Experimental phantom of two objects moved away from the optical detection plane (D) at four positions. (b) Recovered object location error. (c) Recovered object diameter FWHM with respect to the x-ray source dimension. (d) Recovered object diameter FWHM with respect to the optical detection dimension.

dimension, as the mean standard deviation of the error in recovered size with respect to depth is 2.4 mm. This larger standard deviation is consistent with object blurring at depth from the optical detector; this is expected due to the ill-posed nature of the algorithms needed for the optical photon modeling. Similar to figure 3(d), this system is able to distinguish between the different-sized objects in the optical dimension, although again, there is a tendency for dilation in the optically resolved dimension.

Overall, the numerical phantom results show localization accuracy with median error of 2.2 mm (mean of 6.3 mm), or 4.1% (mean of 11.5%) of object depth for all lesions. The recovered lesion size has lower size-bias, with median error of -8.1% versus 87.5% (mean of 19.4% and 118.3%, respectively), in the x-ray excitation direction versus the optical direction, respectively. Again, this optical dilation is expected due to the increased optical scatter compared to x-ray. This technique is invariant in recovered size with respect to depth, as the standard deviation is less than 2.5 mm.

The concentration phantom is shown in figure 5(a). The required dose (in Gy) to reach an SNR of 10 is plotted for varying concentrations. It is apparent from this calculation that a 6 mm diameter object with μg ml^{-1} concentration is detectable in this geometry with standard CT doses. With the doses currently used in IORT, concentrations to ng ml^{-1} are detectable at depth. As shown in figure 5(b), with sufficient signal, contrast can be recovered for all contrast to background ratios tested, for depths up to 45 mm. Here, the advantage of the ability of the collimated x-ray to selectively excite the phosphors is clear.

3.2. Experimental phantom results

Photographs of the experimental phantom are shown in figure 6; the schematic of the experimental phantom is shown in figure 7(a), and the results are shown in figures 7(b)–(d).

(a)
(b)
(c)
(d)

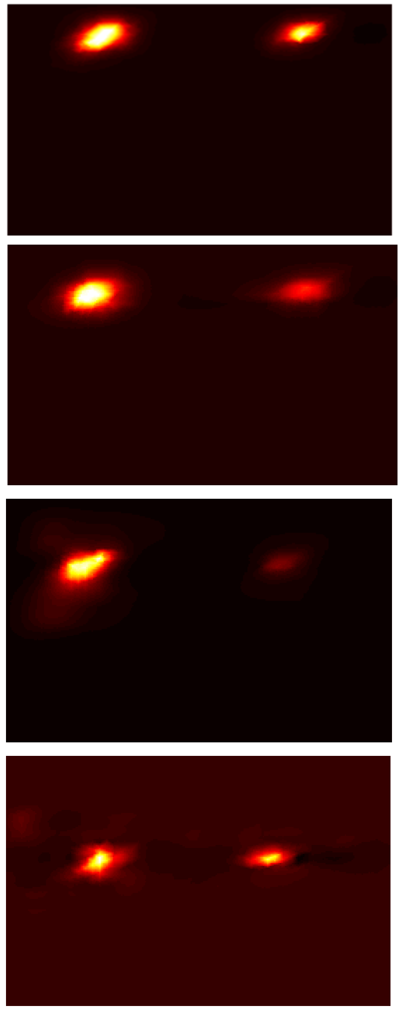

Figure 8. Image reconstructions of two objects with depths of (a) 10, (b) 15, (c) 20 and (d) 30 mm from the detection plane.

Reconstructions for each case are shown in figure 8, with increasing depth with each row. In this experiment, a 1–5 mm object, and a 1–10 mm object were imaged at various depths. For all depths, the recovered location error for both objects is less than 6 mm, and is independent of object size. Positional errors are recovered within 8.6% of the effective depth for a 5 mm object, and within 5.2% of the depth for a 10 mm object. Similar to the results from the numerical phantom, the ability to discern object size is highly accurate in the x-ray dimension, and is invariant with depth. The ability to resolve the object in the optical dimension is accurate to within 2 mm. Object-size median error is within 2.3% and 2% for the 5 mm and 10 mm objects, respectively.

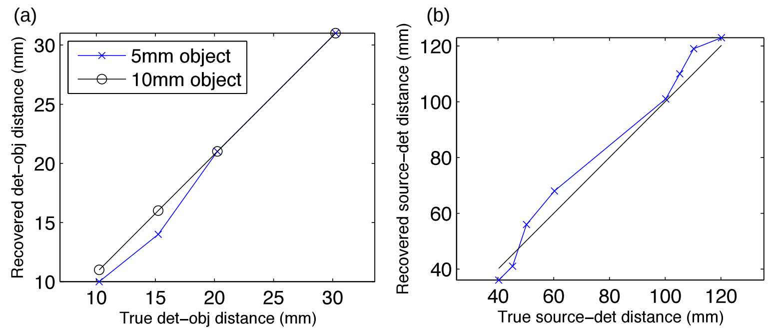

Figure 9. (a) Object location linearity of the depth of the object with respect to the detection plane. (b) Object location linearity of both the depth of the object with respect to the detection plane summed with distance with respect to the source plane.

4. Discussion

Molecular imaging has long been identified as potentially a vital tool in surgery to aid in the identification of important tissue structures and tumor tissue (Gregorie *et al* 1968). Until recently, the use of molecular imaging in surgery has been limited, both due to the lack of appropriate imaging tools, as well as the lack of highly specific contrast agents (the problem with most endogenous fluorescence agents in the body). Recent developments in both of these areas have increased the interest of molecular surgical guidance (Weissleder and Pittet 2008). For instance, fluorescence molecular tomography (FMT) shows great promise in positively affecting surgical outcomes, as it is non-ionizing, has a wealth of knowledge of contrast agents, and can be implemented at low cost. FMT has found utility in tumor-margin excision (Stummer *et al* 2000), sentinel lymph-node mapping (Tanaka *et al* 2006), and avoidance of critical structures such as nerves (Boyette *et al* 2007). Alternatively, sentinel lymph-node identification with radio-emission imaging is widely adopted (Alex and Krag 1993); its use in surgical resection is not well established.

The lack of wide adoption of molecular imaging in surgical applications can partly be blamed on the limited flexibility of these imaging technologies. While FMT is ideal for structures at the surface and several millimeters beyond, its limitations in depth penetration preclude its ability to unmask disease that exists several centimeters beneath the surface. Radio-emission imaging is limited because of the need to image gamma photons which are highly penetrating in tissue—this prevents the identification of lesion depth, and increases the burden on the surgeon to patiently dig through the tissue until the object is identified. In the case of a sub-millimeter-sized tumor tissue, this practice would be overly laborious.

Clearly, a void exits in the ability of molecular instrumentation to resolve millimeter or sub-millimeter objects at depths of several centimeters. LAXLT may be able to fill this void. Its advantage is the ability to resolve objects at several centimeters of deep. Figure 9 demonstrates this ability, as it is shown that both the 5 mm and 10 mm objects in the experimental phantom were able to be resolved at a detector–object depth of beyond 3 cm. This is a stark contrast to FMT, as Kepshire *et al* (2007) demonstrated that depth linearity degrades beyond 1 cm. If the depth penetration of the x-ray source is considered, LAXLT is linear beyond 10 cm. This increased performance is due to the low scatter and high penetrability of the x-ray excitation, which allows more ideal imaging geometries to be chosen for surgical guidance.

The benefit of the technique developed in this study compared to previous developments with XLT is threefold: increased temporal resolution is possible because of the optical read-out of two dimensions, which eliminates x-ray encoding in those dimensions; lower dose is possible because of the decreased x-ray excitation. Most importantly, this technique is suitable for geometries where full angular x-ray encoding is not possible. Therefore, this technique enables XLT to be used for surgeries such as breast lumpectomy; we foresee applications such as this to be one of the most important future applications in imaging. In breast lumpectomy, a full-angular encoding with x-ray is not desirable because deep critical structures are irradiated. By instead implementing a limited-angle technique, only the breast may be irradiated. For lumpectomy, this technique would be desirable to verify the position of the lesions in the surgical supine position, and to visualize remaining disease after resection.

In comparing this technique to other image-guided surgical modalities such as FMT, the advantages of LAXLT are clear. LAXLT was able to resolve 4 mm objects at detector–object depths greater than 4.5 cm, compared to FMT which is limited in to about 1 cm in resolving object dimensions (Kepshire *et al* 2007). The most impressive aspect indicated by these results is the reduction in the blurring of the object with respect to depth; this highlights the advantage of incorporating the x-ray excitation, which due to its relatively insignificant scatter at these depths can pinpoint the depth of the object with respect to the optical depth dimension. The optical read-out is then used to determine the other dimensions. Since the depth is known to high accuracy (shown in figure 4), the diffuse algorithm properly models the diffuse nature of the light, and significantly reduces object blurring, as presented in figure 5. Thus, with LAXLT, dose and imaging time are reduced significantly compared to XLT.

It is intuitive that the resolution will be limited by the width of the x-ray beam, at shallower depths. At deeper depths, the scatter of the x-ray beam should be taken into account. In this study, a 1 mm collimated x-ray beam was able to successfully visualize a 2 mm object up to 2 cm, and a 4 mm object up to 4.5 cm. Higher resolution should be attained with a narrower beam; we are currently investigating this effect. The ability to resolve an object at depth is instead limited by dose.

Although this study was adapted to geometries best suitable to tumor resection, it should be noted that the algorithm presented in this work is generalizable to any geometry; it is especially useful for sparse-angle geometries. An additional use for this technique would be for intraoperative probes, where simple coregistration (assuming the catheter is radio-opaque) between the x-ray source and the optical detection catheter could provide assessment of molecular status at a remote location.

An increase in dose to potentially healthy tissue is one disadvantage of this technique. Although we calculated that the maximum dose to the phantom was 33.4 cGy, this dose will be reduced to 6 cGy with a more favorable optical setup where the camera is closer to the object. This dose may be reduced further with a contact optical setup. Still, this dose may preclude its use in a screening setting, especially due to the increasing awareness of increasing radiation exposure in medicine (Caoili *et al* 2009). However, post-surgical radiation therapy is commonly prescribed as a means to destroy cancer cells that may not have been removed around the margin (Dirbas 2009, Munshi 2007). In accelerated partial breast irradiation, 5–20 Gy of radiation is given to the resected cavity in 1–5 fractions, to reduce the morbidity of whole breast radiation therapy (Ross 2005). In this context, LAXLT may have great utility to identify larger regions that may have been missed during surgery, and may require subsequent surgical investigation. Its sensitivity at this dose might enable the identification of micro-disease, or a very low concentration to be injected.

The other disadvantage of this technique is its use of nanoparticles. Although we have demonstrated low toxicity of our nanoparticles in cells, nanoparticles will have different

effects in a living system. This topic is beyond the scope of this paper, but it is important to recognize that cancer nanotechnology is a major venture in the National Cancer Institute, and this technique will benefit from the knowledge gained from this program.

5. Conclusions

LAXLT has been developed as a means to image molecular deeper than is available with FMT. A reconstruction algorithm, based on a hybrid x-ray excitation/diffuse optical emission model, was tested in a numerical and experimental phantom that had dimensions similar to the human breast. It was found that objects as small as 2 mm in diameter could be resolved at depths of up to 4–5 cm. It was shown that the depth of the object with respect to the x-ray source position had little effect on object recovery in this volume. It was then demonstrated experimentally that both a 5 and 10 mm object could be resolved at depths of at least 3 cm; these results agreed with the numerical phantom results, thus validating the simulation. If the challenges to engineering biocompatible phosphors can be resolved, LAXLT may have utility in surgical applications where small lesions must be imaged at depth of a few centimeters, such as during breast lumpectomy surgery.

Acknowledgments

The authors gratefully acknowledge the Department of Defense Breast Cancer Postdoctoral Fellowships W81XWH-10-1-0506 (CMC), W81XWH-11-1-0070 (GP), and W81XWH-11-1-0087 (CS), the National Institutes of Health ICMIC P50CA114747, the Center for Biomedical Imaging at Stanford, and the Friends for Early Breast Cancer Detection, for funding.

References

Q2

Alex J C and Krag D N 1993 Gamma-probe guided localization of lymph nodes *Surg. Oncol.* **2** 137–43

Aronson R 1995 Boundary-conditions for diffusion of light *J. Opt. Soc. Am.* A **12** 2532–9

Arridge S R, Schweiger M, Hiraoka M and Delpy D T 1993 A finite-element approach for modeling photon transport in tissue *Med. Phys.* **20** 299–309

Barrett H H 1990 Limited-angle tomography for the nineties (comment) *J. Nucl. Med.* **31** 1688–92

Boyette L B, Reardon M A, Mirelman A J, Kirkley T D, Lysiak J J, Tuttle J B and Steers W D 2007 Fiberoptic imaging of cavernous nerves *in vivo* *J. Urol.* **178** 2694–700

Caoili E M, Cohan R H, Ellis J H, Dillman J, Schipper M J and Francis I R 2009 Medical decision making regarding computed tomographic radiation dose and associated risk: the patient's perspective *Arch. Intern. Med.* **169** 1069–71

Carpenter C, Sun C, Pratx G, Rao R and Xing L 2010 Hybrid x-ray/optical luminescence imaging; characterization of experimental conditions *Med. Phys.* **37** 4011

Chen W 2008 Nanoparticle fluorescence based technology for biological applications *J. Nanosci. Nanotechnol.* **8** 1019–51

Chen X, Conti P S and Moats R A 2004 *In vivo* near-infrared fluorescence imaging of integrin alphavbeta3 in brain tumor xenografts *Cancer Res.* **64** 8009–14

Cheong W F, Prahl S A and Welch A J 1990 A review of the optical properties of biological tissues *IEEE J. Quantum Electron.* **26** 2166–85

Dirbas F M 2009 Accelerated partial breast irradiation: where do we stand? *J. Natl Compr. Cancer Netw.* **7** 215–25

Fortin A, Larochelle M, Laverdière J, Lavertu S and Tremblay D 1999 Local failure is responsible for the decrease in survival for patients with breast cancer treated with conservative surgery and postoperative radiotherapy *J. Clin. Oncol.* **17** 101–9

Gibson G R, Lesnikoski B A, Yoo J, Mott L A, Cady B and Barth R J Jr 2001 A comparison of ink-directed and traditional whole-cavity re-excision for breast lumpectomy specimens with positive margins *Ann. Surg. Oncol.* **8** 693–704

Gregorie H B Jr, Horger E O, Ward J L, Green J F, Richards T, Robertson H C Jr and Stevenson T B 1968 Hematoporphyrin-derivative fluorescence in malignant neoplasms *Ann. Surg.* **167** 820–8

Haubner R, Wester H J, Weber W A, Mang C, Ziegler S I, Goodman S L, Senekowitsch-Schmidtke R, Kessler H and Schwaiger M 2001 Noninvasive imaging of alpha(v)beta3 integrin expression using 18F-labeled RGD-containing glycopeptide and positron emission tomography *Cancer Res.* **61** 1781–5

Jiang H B 1998 Frequency-domain fluorescent diffusion tomography: a finite-element-based algorithm and simulations *Appl. Opt.* **37** 5337–43

Kandarakis I, Cavouras D, Panayiotakis G, Agelis T, Nomicos C and Giakoumakis G 1996 X-ray induced luminescence and spatial resolution of La2O2S:Tb phosphor screens *Phys. Med. Biol.* **41** 297–307

Kepshire D S, Davis S C, Dehghani H, Paulsen K D and Pogue B W 2007 Subsurface diffuse optical tomography can localize absorber and fluorescent objects but recovered image sensitivity is nonlinear with depth *Appl. Opt.* **46** 1669–78

Ma C M, Coffey C W, DeWerd L A, Liu C, Nath R, Seltzer S M, Seuntjens J P and American Association of Physicists in Medicine 2001 AAPM protocol for 40–300 kV x-ray beam dosimetry in radiotherapy and radiobiology *Med. Phys.* **28** 868–93

Marquardt D W 1963 An algorithm for least-squares estimation of nonlinear parameters *J. Soc. Indust. Appl. Math.* **11** 431–41

Munck af Rosenschöld P, Nilsson P and Knöös T 2008 Kilovoltage x-ray dosimetry—an experimental comparison between different dosimetry protocols *Phys. Med. Biol.* **53** 4431–42

Munshi A 2007 External hypofractionated whole-breast radiotherapy: now where does accelerated partial breast irradiation stand? *J. Cancer Res. Ther.* **3** 231–5

O'Leary M A, Boas D A, Chance B and Yodh A G 1995 Experimental images of heterogeneous turbid media by frequency-domain diffusing-photon tomography *Opt. Lett.* **20** 426–8

Peters V G, Wyman D R, Patterson M S and Frank G L 1990 Optical properties of normal and diseased human breast tissues in the visible and near infrared *Phys. Med. Biol.* **35** 1317–34

Pratx G, Carpenter C, Sun C, Ravilisetty P and Xing L 2010a Tomographic molecular imaging using x-ray-excitable nanoparticles *Opt. Lett.* **35** 3345–7

Pratx G, Carpenter C, Sun C and Xing L 2010b X-ray luminescence computed tomography via selective excitation: a feasibility study *IEEE Trans. Med. Imaging* **29** 1992–9

Roberts D W *et al* 2010 Coregistered fluorescence-enhanced tumor resection of malignant glioma: relationships between delta-aminolevulinic acid-induced protoporphyrin IX fluorescence, magnetic resonance imaging enhancement, and neuropathological parameters *J. Neurosurg.* **Q3**

Ross G 2005 Accelerated partial breast irradiation: technically feasible but who will benefit? *Breast Cancer Res.* **7** 110–2

Schweiger M, Arridge S R, Hiraoka M and Delpy D T 1995 The finite element method for the propagation of light in scattering media: boundary and source conditions *Med. Phys.* **22** 1779–92

Sokolov K, Follen M, Aaron J, Pavlova I, Malpica A, Lotan R and Richards-Kortum R 2003 Real-time vital optical imaging of precancer using anti-epidermal growth factor receptor antibodies conjugated to gold nanoparticles *Cancer Res.* **63** 1999–2004

Stummer W, Novotny A, Stepp H, Goetz C, Bise K and Reulen H J 2000 Fluorescence-guided resection of glioblastoma multiforme by using 5-aminolevulinic acid-induced porphyrins: a prospective study in 52 consecutive patients *J. Neurosurg.* **93** 1003–13

Stummer W *et al* and ALA-Glioma Study Group 2008 Extent of resection and survival in glioblastoma multiforme: identification of and adjustment for bias *Neurosurgery* **62** 564–76 discussion

Sun C, Carpenter C, Pratx G and Xing L 2010 Facile synthesis of amine-functionalized Eu3+-Doped La(OH)3 nanophosphors for bioimaging *Nanoscale Res. Lett.*

Tanaka E, Choi H S, Fujii H, Bawendi M G and Frangioni J V 2006 Image-guided oncologic surgery using invisible light: completed pre-clinical development for sentinel lymph node mapping *Ann. Surg. Oncol.* **13** 1671–81

Torzilli G, Takayama T, Hui A M, Kubota K, Harihara Y and Makuuchi M 1999 A new technical aspect of ultrasound-guided liver surgery *Am. J. Surg.* **178** 341–3

Verhaegen F, Nahum A E, Van de Putte S and Namito Y 1999 Monte Carlo modelling of radiotherapy kV x-ray units *Phys. Med. Biol.* **44** 1767–89

Weissleder R and Pittet M J 2008 Imaging in the era of molecular oncology *Nature* **452** 580–9